

The Galactic metallicity gradient shown by open clusters in the light of radial migration

Martin Netopil,¹★ İnci Akkaya Oralhan,² Hikmet Çakmak,³ Raúl Michel,⁴ Yüksel Karataş³

¹*Kuffner Observatory, Johann-Staud-Straße 10, A-1160 Wien, Austria*

²*Department of Astronomy and Space Sciences, Science Faculty, Erciyes University, TR-38039, Kayseri, Turkey*

³*Department of Astronomy and Space Sciences, Science Faculty, Istanbul University, TR-34116, Üniversite-Istanbul, Turkey*

⁴*Observatorio Astronómico Nacional, Universidad Nacional Autónoma de México, Apartado Postal 877, C.P. 22800, Ensenada, B.C., México*

Accepted 2021 October 10. Received 2021 October 10; in original form 2021 April 20

ABSTRACT

During the last years and decades several individual studies and large-scale spectroscopic surveys significantly improved our knowledge of the Galactic metallicity distribution based on open clusters. The availability of *Gaia* data provided a further step forward in our knowledge. However, still some open issues remain, for example the influence of radial migration on the interpretation of the observed gradients. We used spectroscopic metallicities from individual studies and from the APOGEE survey to compile a sample of 136 open clusters, with a membership verification based on *Gaia* DR2. Additionally, we present photometric metallicity estimates of 14 open clusters in a somewhat outer Galactic region. Eight age groups allow us to study the evolution of the metallicity gradient in detail, showing within the errors an almost constant gradient of about -0.06 dex kpc⁻¹. Furthermore, using the derived gradients and an analysis of the individual objects, we estimate a mean migration rate of 1 kpc Gyr⁻¹ for objects up to about 2 Gyr. Here, the change of the guiding radius is clearly the main contributor. For older and dynamically hotter objects up to 6 Gyr we infer a lower migration rate of up to 0.5 kpc Gyr⁻¹. The influence of epicyclic excursions increases with age and contributes already about 1 kpc to the total migration distance after 6 Gyr. A comparison of our results with available models shows good agreement. However, there is still a lack of a suitable coverage of older objects, future studies are still needed to provide a better sampling in this respect.

Key words: techniques: photometric – techniques: spectroscopic – Galaxy: abundances – open clusters and associations: general

1 INTRODUCTION

Open clusters provide the unique possibility to derive reliable parameters based on their numerous member stars that generally share the same properties. Open clusters therefore represent invaluable objects for numerous topics related to evolutionary studies. In case of the Galactic metallicity gradient and its evolution, to our best knowledge the first study dates back to [Janes \(1979\)](#). He used photometric data to identify a metallicity gradient of about -0.05 dex kpc⁻¹ and that a younger population shows a shallower gradient than an older one. However, he notes that the age dependence could be also a bias because of the objects' distribution. The existence of a metallicity gradient was consolidated in the last decades even by using larger data sets and by switching to spectroscopic measurements, the evolution of the gradient, however, is still debatable. An overview of literature results for different tracers is presented by [Anders et al. \(2017\)](#).

Though, still some other open questions remain. For example, is there some evidence of a transition zone in the Milky Way that splits the disc into two regions with different metallicity gradients? [Lépine et al. \(2011\)](#) even conclude two shallow plateaus with a step-like discontinuity. Recently, [Monteiro et al. \(2021\)](#) identified a flattening of

the gradient at a galactocentric distance (R_{GC}) of about 10 kpc. Furthermore, they note that the corotation radius, the strongest Galactic resonance close to the solar circle, divides the Galaxy into two parts with independent chemical evolution and causes a gap of the cluster distribution in the range $8.5 \text{ kpc} \leq R_{GC} \leq 9.5 \text{ kpc}$.

The increasing number of available objects allowed to split the available open cluster samples into several age groups to investigate age-metallicity relations in more detail. A shift of the metallicity level with age in young and intermediate-age open clusters is noted in several works (e.g. [Jacobson et al. 2016](#); [Netopil et al. 2016](#); [Donor et al. 2020](#); [Spina et al. 2021](#)) or can be inferred from the presented data. It was interpreted e.g. by [Netopil et al. \(2016\)](#) as a result of radial mixing. This metallicity shift is not supported by available chemodynamical models (e.g. [Minchev et al. 2013](#)), but [Jacobson et al. \(2016\)](#) outlined the variations of different models and their strong sensitivity to the adopted input parameters. [Anders et al. \(2017\)](#) on the other hand proposed a mechanism including radial mixing and cluster disruption to explain the observations of open clusters. They conclude that non- or inward-migrating clusters might be more prone to disruption, leading to an appearance of metal-rich clusters in the solar neighbourhood (which migrated from inwards) and resulting in a steeper gradient for intermediate-age clusters. However, we also have to deal with some limitation of the chemical abundances itself - the lower metallicity of young objects

★ E-mail: mn.netopil@gmail.com

was recently explained by problems in the spectroscopic analysis (e.g. [Baratella et al. 2020](#); [Spina et al. 2021](#)).

The interpretation of the radial metallicity distribution is generally influenced by several factors. From the observational side these are clearly the reliability of the objects’ distance, age and metallicity. However, meanwhile we know that stars (and open clusters) migrate in the Galaxy by a combination of orbital heating and diffusion of orbital angular momentum. These two effects, often also denoted as “blurring” for the epicyclic excursions and “churning” for changes of the guiding radius (see e.g. [Sellwood & Binney 2002](#); [Schönrich & Binney 2009](#)), result in an additional scatter of the radial metallicity distribution. Its interpretation therefore requires on the one hand accurate cluster parameters, and on the other hand the use of mono-age populations with a sufficiently small age range to obtain some idea about possible variations of the radial migration efficiency by a comparison of these populations.

[Netopil et al. \(2016\)](#) presented a set of mean open cluster metallicities by combining individual spectroscopic measurements on the star level. The sample was divided into two quality categories according to spectroscopic resolution and signal-to-noise ratio, but also includes a set of photometric determinations. The spectroscopic data of 100 objects were used to study the radial metallicity distribution and the age–metallicity relation, and provide a possible observational evidence for radial migration. A main improvement to the work by [Netopil et al. \(2016\)](#) is that thanks to *Gaia* DR2 data a more accurate revision of the cluster star membership was possible, which removed eight objects from their sample. Some additional distant objects were added by following their procedure. Furthermore, also the distance and age scale of the open clusters was completely revised.

The first intention of this paper was to improve our knowledge of the transition radius by adding 14 open clusters to the data set by [Netopil et al. \(2016\)](#). These are located in a somewhat outer Galactic region ($R_{GC} \sim 10\text{--}12$ kpc) and were analysed with a photometric method introduced by [Pöhl & Paunzen \(2010\)](#). During preparation of this paper, another large data set of open cluster metallicities was published ([Donor et al. 2020](#)) that allowed us to tackle the other mentioned issues as well, in particular the age dependence of the radial [Fe/H] gradient and the influence of radial migration.

This paper is arranged as follows: In Sect. 2 and 3, we describe the photometric observations and analysis of 14 open clusters. In Sect. 4, we compile spectroscopic metallicities of open clusters, and in Sect. 5, we discuss the Galactic distribution of the samples, the age dependence of the metallicity gradients, and provide an estimate of the radial migration rate. Finally, Sect. 6 summarizes this paper.

2 OBSERVATIONS AND DATA REDUCTION

The observations of 14 open clusters were carried out at the San Pedro Martir Observatory (SPMO) during photometric nights in the years 2002–2019 using the 0.84-m (f/15) Ritchey–Chrétien telescope, which is equipped with the Mexman filter wheel and the ESOPO CCD detector. The ESOPO detector, a 2048×2048 $13.5\text{-}\mu\text{m}$ square pixels E2V CCD42-40, has a gain of $1.65\text{ e}^-/\text{ADU}$ and a readout noise 3.8 e^- at 2×2 binning. The combination of telescope and detector provides an unvignetted field of view of $7.4 \times 9.3\text{ arcmin}^2$.

Each open cluster was observed at very good seeing conditions ($0''.6$ in long V exposure images) through the Johnson’s UBV and the Kron–Cousins’ RI filters with short and long exposure times to properly cover both, bright and faint stars in the region. Standard star fields ([Landolt 2009](#)) were observed at the meridian and at about two airmasses to properly determine the atmospheric extinction coeffi-

cients. The observation log is provided as supplementary material. Flat fields were taken at the beginning and the end of each night, and bias images were obtained between the cluster observations. Data reduction was carried out by one of the authors (RM) with the IRAF/DAOPHOT¹ package ([Stetson 1987](#)).

The standard magnitude for a given filter λ was derived using the following relation:

$$M_\lambda = m_\lambda - k_\lambda X + \eta_\lambda C + \zeta_\lambda, \quad (1)$$

where m_λ , k_λ , C and X are the observed instrumental magnitude, extinction coefficients, colour index, and air mass, respectively. M_λ , η_λ , and ζ_λ are the standard magnitude, transformation coefficient, and photometric zero point, respectively. More details about the data reduction can be found in the papers by [Akkaya Oralhan et al. \(2010, 2015, 2019, 2020\)](#), [Schuster et al. \(2007\)](#), [Tapia et al. \(2010\)](#).

3 OPEN CLUSTER ANALYSIS

3.1 Membership

The $UBVR_I$ photometric data of the open clusters have been combined with *Gaia* DR2 ([Gaia Collaboration et al. 2018a](#)) proper motion and parallax data to select the most likely cluster members. As a quite typical example, the distribution in μ_α, μ_δ (vector point diagram, VPD) of the cluster stars in Basel 4 is shown in Fig. 1. The potential cluster members show a more concentrated structure, whereas field stars (grey dots) have a more scattered distribution. The membership probabilities P (per cent) of the cluster stars have been determined using a Gaussian Mixture Model (GMM; [Pedregosa et al. 2011](#)). The first rise in the P histograms of the clusters are taken as criteria for the cluster membership limit. In the case of Basel 4, stars with $P \geq 80$ per cent (vertical dashed line of panel b) are considered to be likely members (filled dots in the VPDs). The same membership procedure has been applied to the remaining open clusters. The GMM² model considers that the distribution of proper motions of the stars in a cluster’s region can be represented by two elliptical bivariate Gaussians. The expressions used can be found in the papers by [Balaguer-Núñez et al. \(1998\)](#), [Wu et al. \(2002\)](#), [Sariya et al. \(2012\)](#) and [Dias et al. \(2018\)](#). The median proper motion components, median parallaxes and P (per cent) cut-off values of the probable members are listed in Table 1. Within the uncertainties the median proper motions and parallax of the likely cluster members are in agreement with the results by [Cantat-Gaudin & Anders \(2020\)](#).

3.2 Open cluster parameters

The used open cluster analysis method was developed by [Pöhl & Paunzen \(2010\)](#), and was applied with some modifications to a larger sample by [Netopil & Paunzen \(2013\)](#). It uses photometric data that are transformed to effective temperatures and luminosities in an iterative way. These are compared to zero-age main-sequence (ZAMS) normalized isochrones (differential grids, DG) to obtain the open

¹ IRAF is distributed by the National Optical Observatories, operated by the Association of Universities for Research in Astronomy, Inc., under cooperative agreement with the National Science Foundation.

² P is defined as Φ_c / Φ . Here $\Phi = \Phi_c + \Phi_f$ is the total probability distribution, where c and f are subscripts for cluster and field parameters, respectively. The used parameters for the estimation of Φ_c and Φ_f are $\mu_\alpha, \mu_\delta, \varpi, \sigma_{\mu_\alpha}, \sigma_{\mu_\delta}, \sigma_\varpi$.

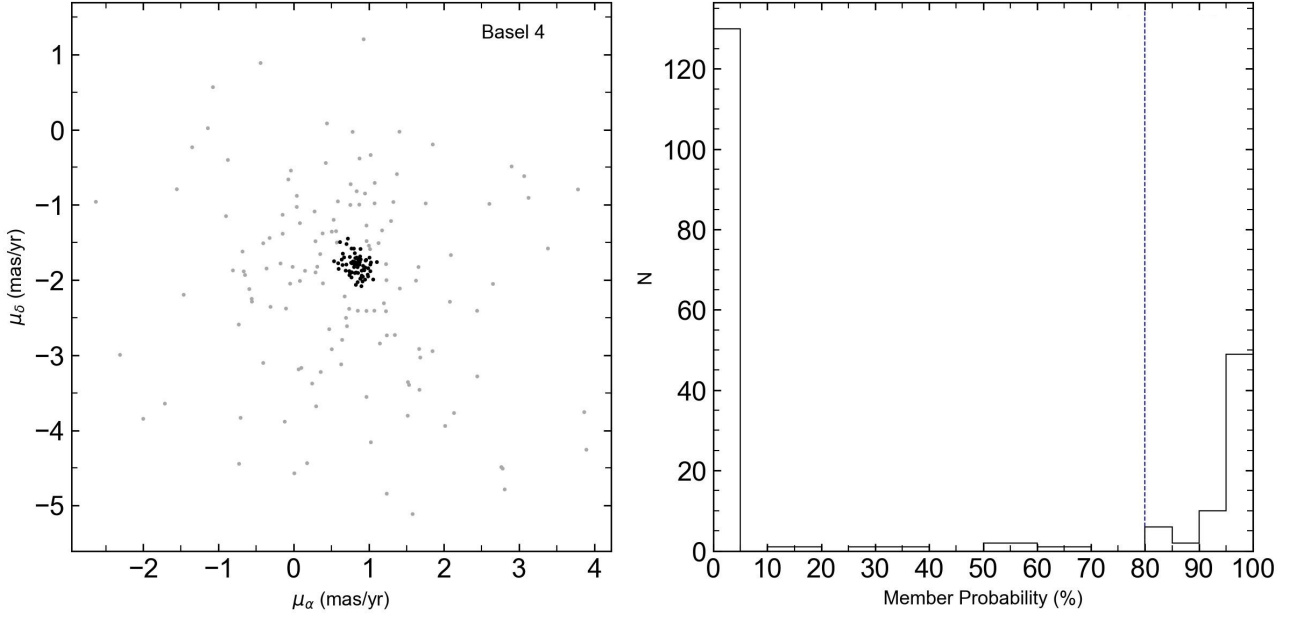


Figure 1. Left-hand panel: the $\mu_\alpha - \mu_\delta$ distribution of stars in Basel 4. Right-hand panel: the membership probability histogram P (per cent). The stars with $P \geq 80$ per cent (vertical blue dashed line) are adopted as the likely cluster members (filled black dots in the VPD).

Table 1. Membership analysis of the open clusters.

Cluster	N	μ_α	σ_{μ_α}	μ_δ	σ_{μ_δ}	ϖ	σ_ϖ	d (kpc)	σ_d	P(per cent)
Basel 4	67	0.846	0.014	-1.804	0.016	0.278	0.009	3.600	0.121	80
Berkeley 35	85	-0.564	0.011	-0.240	0.012	0.170	0.008	5.893	0.264	85
Berkeley 60	94	-0.666	0.013	-0.720	0.011	0.230	0.008	4.347	0.153	80
Berkeley 77	56	-0.976	0.014	-0.131	0.019	0.259	0.012	3.856	0.183	80
Berkeley 104	53	-2.399	0.025	0.097	0.020	0.191	0.011	5.244	0.307	80
Haffner 4	77	-0.406	0.021	0.927	0.020	0.209	0.010	4.786	0.222	80
King 15	67	-2.334	0.020	-0.823	0.017	0.308	0.010	3.252	0.101	70
King 23	54	-0.444	0.017	-0.895	0.013	0.272	0.008	3.683	0.110	85
NGC 1857	105	0.560	0.011	-1.307	0.010	0.339	0.006	2.952	0.053	80
NGC 2186	106	0.398	0.014	-1.977	0.025	0.409	0.009	2.447	0.052	75
NGC 2236	226	-0.746	0.012	0.017	0.011	0.357	0.005	2.799	0.042	70
NGC 2259	126	-0.247	0.018	-1.117	0.017	0.310	0.012	3.230	0.129	70
NGC 2304	102	-0.029	0.016	-1.548	0.020	0.198	0.008	5.063	0.199	75
NGC 2383	264	-1.642	0.007	1.899	0.008	0.308	0.006	3.252	0.064	70

Notes. Gaia DR2 proper motion components (mas yr^{-1}), parallax (mas), and distances (kpc) of the likely members in the programme clusters. The chosen lower limit of membership probabilities, P (per cent) are given in last column.

cluster parameters, including metallicity. For more details we refer to the two references above, but we want to emphasize here the main advantages of the method: it relies on the complete cluster MS and allows to incorporate many photometric systems and colours to improve the reliability of the results.

Netopil & Paunzen (2013) have shown that the results for metallicity are independent of the used evolutionary models, the resulting Z values just need to be correctly transformed into the corresponding $[\text{Fe}/\text{H}]$ values, the most common used indication of metallicity. Though we note that in case of non-solar scaled abundances, the calibrated $[\text{Fe}/\text{H}]$ value might deviate from the actual iron abundance.

For this study, we calculated new differential grids, because the

previously used ones are available only in quite large steps in age ($\Delta \log t = 0.2$) and luminosity ($\Delta L/L_\odot = 0.3$) and rely on an already outdated solar abundance ($Z = 0.02$). We adopt the version 1.2S of the PARSEC tracks (Bressan et al. 2012)³, which were computed for a scaled-solar composition with $Z_\odot = 0.0152$. The ZAMS was constructed using the to the solar value closest available track ($Z = 0.014$) and isochrones were obtained for seven metallicities ($Z=0.004, 0.006, 0.010, 0.014, 0.020, 0.030$, and 0.040) with age steps $\Delta \log t = 0.05$. Finally, the differential grids were derived in

³ <http://stev.oapd.inaf.it/cgi-bin/cmd>

luminosity steps of 0.1 dex from $L/L_{\odot} = 0.0$ up to the end of the MS.

Some additional improvements in deriving effective temperatures and luminosities of the cluster stars as input to the analysis method rely on the work by [Pecaut & Mamajek \(2013\)](#) and their updated Table 5⁴. We adopt their results for the bolometric correction instead of the one by [Flower \(1996\)](#). Furthermore, their photometric colours of the dwarfs effective temperature sequence were used to adjust possible temperature offsets in the compiled photometric temperature calibrations. We noticed that the calibration for the $(V-R)_C$ colour by [Netopil & Paunzen \(2013\)](#) resulted in too hot temperatures because of a sign error in the transformation between the different $(V-R)$ systems. The correct temperature calibration to match also the scale by [Pecaut & Mamajek \(2013\)](#) is

$$\theta_{\text{eff}} = 0.536(3) + 0.947(13)(V-R)_C. \quad (2)$$

The effective temperatures based on the other colours agree very well with the temperature sequence by [Pecaut & Mamajek \(2013\)](#) at a 0.01-mag level. Finally, we added their temperature sequence for *Gaia* photometry ($G_{BP} - G_{RP}$); thus, the derived mean effective temperatures are based on up to five colour indices: using our photometric data, 2MASS ([Skrutskie et al. 2006](#)) or UKIDSS ([Lucas et al. 2008](#)) K magnitudes, and the *Gaia* colour index. The latter colour was dereddened using extinction coefficients as a function of interstellar absorption A_V and the colour ($G_{BP} - G_{RP}$) as suggested by [Gaia Collaboration et al. \(2018b\)](#). For the total-to-selective extinction ratio, we adopt a standard value $R_V = 3.1$ to avoid an additional free parameter in the open cluster analysis.

The comparison of the temperature scales based on the individual colours and the colour–colour transformations between *Gaia* and *VRI* data ([Evans et al. 2018](#)) allow to evaluate possible offsets of our photometric data (see Table A1). We noticed a good agreement between these two approaches for $(V-I)$, but found a disagreement for $(V-R)$, depending on the cluster reddening. The difference increases up to about 0.08 mag for the highest reddened cluster (Berkeley 60). This might be related to the colour excess ratio $E(V-R)/E(B-V)$ given by [Bessell et al. \(1998\)](#), but also to reddening or metallicity effects in the colour–colour transformations. We note that $(V-I)$ shows none or little blanketing effects compared to $(V-R)$ (see e.g. [Alonso et al. 1996](#)). However, using the offsets based on the temperature scale, we noticed a good agreement if fitting isochrones to the individual CMDs.

As starting values for the open cluster analysis we used a mix of *Gaia* based distances by [Cantat-Gaudin & Anders \(2020\)](#), the parameter estimates by [Cantat-Gaudin et al. \(2020\)](#), and our extinction values based on the ZAMS fitting. For the least known parameter metallicity we initially adopt the solar value. The starting values were altered in an iterative procedure until the best fit with the derived differential grids was found (lowest σ over the complete luminosity range). The choice of the starting values has no influence on the final results, but reduces in ideal circumstances the number of iterations. A consistency check of the parameter results was performed by applying PARSEC isochrones to all available CMDs. The derived Z values were transformed to $[\text{Fe}/\text{H}]$ using the relation $\log(Z/X) - \log(Z/X)_{\odot}$, with $(Z/X)_{\odot} = 0.0207$ and $Y = 0.2485 + 1.78Z$ ([Bressan et al. 2012](#)). All results for the open clusters are listed in Table 2, and as an example we present the fits for Basel 4 in Fig. 2. For the remaining open clusters we refer to the Figs. A2 – A14. For most objects, the derived parameters also provide a reasonable fit of the isochrones to

the CMDs. However, differential reddening and also the fixed R_V value in the analysis might lead to apparent offsets in some colours (see e.g. Berkeley 60 in Fig. A3).

The applied method identifies the most reasonable result for the Z -parameter with the lowest scatter over the complete luminosity range; thus, the errors of the remaining cluster parameters (reddening, distance, and age) are not straightforward to indicate. Though, based on the iteration process we conclude that the errors are generally within two iteration steps for the age and distance and within three iteration steps for the reddening; thus, 0.1 dex for the age, 0.1 mag for the distance modulus, and 0.03 mag for the reddening.

Spectroscopic metallicities were recently presented by [Donor et al. \(2020\)](#) for three programme clusters using the SDSS/APOGEE survey. They quote $[\text{Fe}/\text{H}] = -0.16, -0.14$, and -0.12 dex for Haffner 4, NGC 1857, and NGC 2304, respectively. The results are in good agreement to our estimates, but on average a few hundreds of dex (0.02) more metal deficient. Eight more clusters in this sample were previously analysed with the DG method, showing an offset of 0.01 ± 0.06 dex (own – APOGEE). Thus, indicating that the change in the analysis used in this study has not altered the previous metallicity scale. This confirms the conclusion by [Netopil & Paunzen \(2013\)](#). Using all clusters in common we derive an offset to the APOGEE results of 0.01 ± 0.05 dex. Prior to this study, almost 70 open clusters were analysed with this method and [Netopil et al. \(2016\)](#) noticed an almost identical accuracy and precision in comparison with their spectroscopic sample.

4 SPECTROSCOPIC METALLICITIES

4.1 Data compilation

In addition to the new metallicity estimates for our sample clusters, we made use of the spectroscopic data listed by [Netopil et al. \(2016\)](#). The list was updated accordingly with additional data, but including only objects beyond the solar circle ($R_{GC} > 9$ kpc) as the solar vicinity is already very well covered. We noticed four clusters in three references: Berkeley 25 and NGC 2243 by [Magrini et al. \(2017\)](#), NGC 1907 and NGC 7245 by [Casamiquela et al. \(2017\)](#), and NGC 2243 by [Carrera et al. \(2019\)](#). The results for Berkeley 25 and few stars in NGC 2243 by [Magrini et al. \(2017\)](#) belong to the lower quality (LQ) data sample as defined by [Netopil et al. \(2016\)](#) due to the signal-to-noise ratio, all others were merged with the high-quality (HQ) sample. Furthermore, the study by [Carrera et al. \(2019\)](#) used APOGEE and GALAH data, but we only adopt their results based on the latter survey for NGC 2243.

[Donor et al. \(2020\)](#) presented an investigation of open clusters using the most recent SDSS/APOGEE data release (DR16) that we adopt instead. They introduced a reliability flag of the results based on visual inspection of the stars' position in the CMD, and we restrict the total sample of 128 open clusters to the high-quality sample of 71 objects. However, we noticed that one of the outermost clusters (Saurer 1) was flagged as potentially unreliable. We checked the position of the star in the CMD, which although is separated from the main bulk of stars, it lies very close to the corresponding isochrone in all available colours (see Fig. 3). We thus keep the result for this cluster in the sample, because its metallicity is very close to the data in the HQ sample as well. The whole APOGEE data set was kept as an independent one, because of its size and homogeneity. However, based on the spectral resolution of APOGEE ($R \sim 22\,500$), it would belong to the LQ sample by [Netopil et al. \(2016\)](#).

The membership of the cluster stars in the APOGEE sample was

⁴ <https://www.pas.rochester.edu/~emamajek> [Version 2019.3.22]

Table 2. Derived parameters of the open clusters.

Cluster	$\log t$ (dex)	$E(B - V)$ (mag)	$(m - M)_0$ (mag)	Z	[Fe/H] (dex)	R_{GC} (kpc)
Basel 4	8.20	0.55	12.50	0.010(3)	-0.18(14)	11.16
Berkeley 35	9.00	0.13	13.50	0.011(2)	-0.13(08)	12.50
Berkeley 60	8.45	0.86	12.85	0.013(3)	-0.06(11)	10.32
Berkeley 77	8.95	0.10	12.80	0.012(3)	-0.09(12)	11.04
Berkeley 104	8.90	0.52	13.10	0.013(4)	-0.06(14)	10.60
Haffner 4	8.65	0.45	13.00	0.011(3)	-0.13(13)	11.06
King 15	8.70	0.54	12.35	0.013(4)	-0.06(14)	9.84
King 23	9.25	0.11	12.55	0.010(2)	-0.18(09)	10.74
NGC 1857	8.45	0.48	12.20	0.012(4)	-0.09(16)	10.71
NGC 2186	7.95	0.31	11.75	0.012(2)	-0.09(08)	10.08
NGC 2236	8.90	0.48	12.10	0.013(3)	-0.06(11)	10.45
NGC 2259	8.60	0.57	12.30	0.011(3)	-0.13(13)	10.73
NGC 2304	9.00	0.05	12.85	0.011(3)	-0.13(13)	11.56
NGC 2383	8.50	0.30	12.50	0.013(3)	-0.06(11)	10.14

Notes. For Z and [Fe/H], the errors of the last significant digits are given in parenthesis. The errors of the other cluster parameters are discussed in the text. These are 0.1 dex for the age, 0.1 mag for distance modulus, and 0.03 mag for $E(B - V)$.

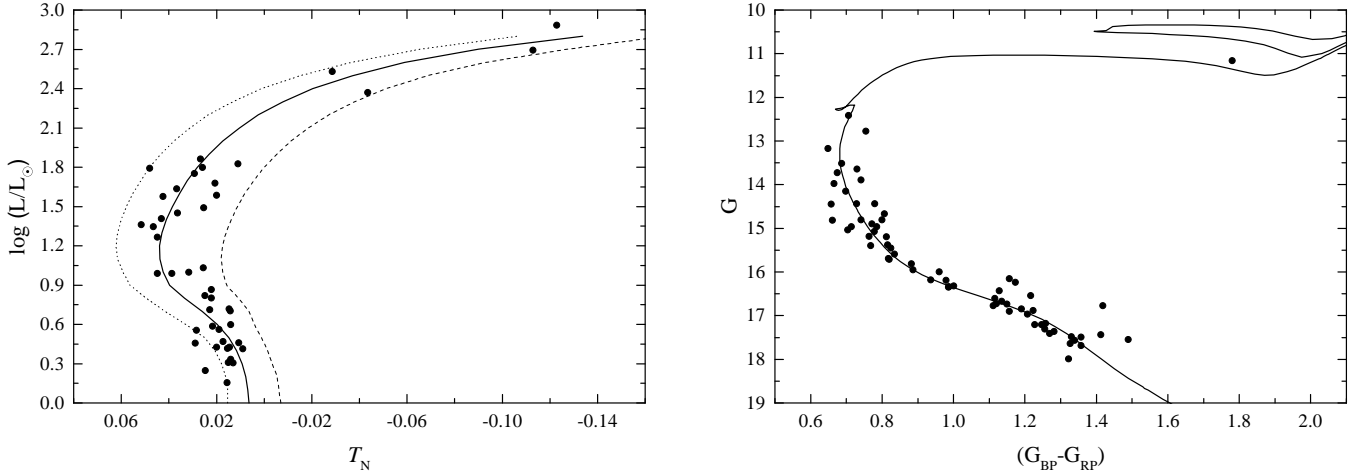


Figure 2. Result for the open cluster Basel 4. The left-hand panel shows the best fit based on the differential grids. The thick line represents the isochrone for $\log t = 8.20$ and $Z=0.01$, the dotted line for $Z=0.006$, and the dashed line for $Z=0.02$. T_N is the temperature difference in dex between the star and the ZAMS at solar metallicity using the mean temperature based on up to five colours. The right-hand panel shows the *Gaia* CMD and an isochrone with the parameters given in Table 2.

already verified using *Gaia* DR2 (Gaia Collaboration et al. 2018a). In the HQ and LQ sample, several cluster results are based on single or few stars, thus it is important to check the cluster membership in these samples as well. We used the membership analysis by Cantat-Gaudin & Anders (2020) and *Gaia* data for not covered objects to conclude about membership based on proper motion, parallax, and radial velocities. This removed six clusters in the HQ sample (Melotte 71, NGC 1545, NGC 1901, NGC 1977, NGC 2266, and NGC 2335) and two objects in the LQ sample (Berkeley 21 and Berkeley 75).

The total sample with spectroscopic metallicities includes 138 open clusters. We compare the individual data sets and derive the following 2σ clipped offsets: 0.05 ± 0.05 (HQ–APOGEE, 24 objects), -0.01 ± 0.07 (LQ–APOGEE, 15 objects), and 0.03 ± 0.08 (HQ–LQ, 31 objects). The two data sets based on medium resolution agree very well, but the HQ data are more metal rich than the

APOGEE results. Though, the offset between the HQ and APOGEE data reduces to about 0.02 dex if using the number of measured stars as a weight. The APOGEE DR16 data include a zero-point shift to force solar metallicity stars in the solar neighbourhood to have a mean $[X/M]=0$ (Jönsson et al. 2020). A similar comparison of clusters close to the solar circle ($7.5 \text{ kpc} < R_{GC} < 8.5 \text{ kpc}$) in all three samples shows a mean metallicity in the range 0.00 ± 0.01 dex. Thus, for the following analysis we do not apply any offsets.

4.2 Distance and age scale

Donor et al. (2020) nicely demonstrated the effect of the distance scale on the analysis of the metallicity gradient. The cluster age is crucial as well, but generally even worse defined than the distance as shown e.g. by Netopil et al. (2015). Thus, it is important to adopt proper cluster parameters. For small samples it is certainly possible to

derive them oneself or check available parameters in a homogeneous way, but for larger samples one has to rely on literature and to decide about the most reliable source.

One can either pick results from numerous individual studies at the expense of homogeneity, or adopt large-scale studies that derived cluster parameters in an automatic way. There are several automatic approaches available (see e.g. Netopil et al. 2015), a recent one by Cantat-Gaudin et al. (2020), who applied an artificial neural network (ANN) on 2D histograms of *Gaia* CMDs using parallax as an additional parameter. Such approaches generally cannot identify individual special features or discrepancies in the parametrization that are noticeable only in a detailed by-eye examination, but a visual inspection of the results as performed e.g. by the latter reference above is usually included.

For this study, we adopt a combination of the two possibilities mentioned above. We use the DG results based on a multicolour analysis (Netopil & Paunzen 2013; Netopil et al. 2016, and this paper) as primary source for 31 clusters in the spectroscopic sample, followed by results from The Bologna Open Clusters Chemical Evolution project (BOCCE, see e.g. Bragaglia & Tosi 2006) for 21 clusters, and Bossini et al. (2019), who used *Gaia* data of 269 selected objects that were analysed with an automated Bayesian tool to fit isochrones. This work covers additional 24 clusters of our sample. The two studies were adopted by Cantat-Gaudin et al. (2020) for the training sample of the ANN. Finally, for the remaining objects we rely on the results by the last reference.

Three clusters from the APOGEE sample are not covered by the selected references (Berkeley 43, FSR 394, and Saurer 1). The first object was flagged by Cantat-Gaudin et al. (2020) as too red, the others are not included (or were rejected) by this survey. We inspected the *Gaia* CMDs and conclude that FSR 394 might be an old distant cluster and Berkeley 43 a highly reddened cluster of intermediate age. However, the large scatter in the CMDs do not allow careful isochrone fits. We therefore rejected the two objects from the sample. Saurer 1, on the other hand, shows a well-defined giant branch and we initially adopt the result by Carraro & Baume (2003), who present deep *VI* photometry of the cluster and derived an age of $\log t = 9.7$.

Finally, we verified the parameters of the 16 most distant (≥ 5 kpc) clusters, corresponding to galactocentric distances of $R_{GC} \geq 12.5$ kpc using *Gaia* CMDs of likely proper motion members and isochrones for metallicities that roughly correspond to the available spectroscopic measurements.

For some objects, such as Saurer 1 or Berkeley 29 (see Figs. 3 and A1), *Gaia* photometry is not deep enough to properly characterize the cluster. In such cases, we queried for additional deeper photometry. Table 3 lists the initial and the adopted parameters after revision. In general, we notice a good agreement, though there are some objects for which the distance differs by about 20 per cent (Berkeley 19, Berkeley 21, Berkeley 22, and Berkeley 25). An excerpt of the physical parameters of the complete open cluster sample is shown in Table 4; the full table is available at the CDS.

4.3 Orbital parameters

Recently, Tarricq et al. (2021) presented orbital parameters for almost 1400 open clusters. Though, they adopted a different solar distance and also the cluster parameters differ to our scale. We thus repeated their calculations using our adopted cluster parameters, a solar distance of $R_{GC} = 8.0$ kpc, the proper motions by Cantat-Gaudin & Anders (2020) and the compiled mean radial velocities by Tarricq et al. (2021).

Three objects are not covered by the latter reference (Berkeley 104,

Ruprecht 4, and Saurer 1) and for six clusters we noticed errors in the radial velocity in the range $8 - 46 \text{ km s}^{-1}$. For these objects we queried the additional literature to adopt the missing or probable more reliable velocities. For the cluster NGC 2194, for example, we adopt $+7.5 \pm 0.8 \text{ km s}^{-1}$ by Jacobson et al. (2011) based on seven objects, while Tarricq et al. (2021) list $+38.7 \pm 8.1 \text{ km s}^{-1}$ based on nine stars. Actually, also *Gaia* data suggest the lower velocity, because of a clustering around $+9 \text{ km s}^{-1}$ of the innermost objects. All of these stars show a proper motion membership probability of 1.0 according to Cantat-Gaudin & Anders (2020); thus, a higher threshold than 0.4 adopted by Tarricq et al. (2021) or some limitation of the radius is required to pinpoint the cluster velocities. It is out of scope of this work to re-evaluate all radial velocities, we therefore stress that this is certainly an invaluable data set for statistical analyses, but might lead to wrong conclusions for probably some individual objects. Only one object remained without a radial velocity estimate, Berkeley 104 from our photometric sample.

The orbital calculations were performed with the PYTHON package GALPY⁵ by Bovy (2015) using the Milky-Way-like potential MWPotential2014, a local rotation velocity of 239 km s^{-1} (Brunthaler et al. 2011) and the solar motion by Schönrich et al. (2010). Each cluster was integrated with an integration step of 0.01 up to 500 Myr at maximum to avoid inaccuracies in the time-dependence of the potential (see discussion by Tarricq et al. 2021).

We obtained among others the orbit boundary information R_{apo} , R_{peri} , z_{max} , the orbits' eccentricity e , and the guiding radii R_{guide} . The latter is the radius of a circular orbit with angular momentum L_z . An excerpt of the orbital parameters are listed in Table 5; the full table is available at the CDS. The eccentricities and galactic plane distances (z_{max}) of our sample clusters reflect the properties of the Galactic thin disc.

5 RESULTS AND DISCUSSION

5.1 Radial metallicity distribution

Figure 4 shows the spectroscopic metallicities as a function of the galactocentric distance R_{GC} , adopting 8.0 kpc as the distance of the Sun from the Galactic Centre for eased comparison with other works (e.g. Netopil et al. 2016; Donor et al. 2020). In total, there are 136 open clusters, 85 and 42 clusters with HQ and LQ data, respectively, and 70 objects covered by the APOGEE survey.

For better clarity, we omit the indication of errors in $[Fe/H]$. We note that these are also not easily comparable as the HQ and LQ compilations include a variety of references that already might introduces a larger scatter, depending on the number of individual references and number of stars involved. The mean error in the HQ and LQ samples is 0.05 and 0.07 dex, respectively, but reach up to 0.13 dex for even well covered objects (e.g. NGC 752 or NGC 3680 in the LQ sample). The APOGEE sample on the other hand is a homogeneous data set that lists errors in the range of 0.01–0.06 dex, apparently adopting the internal error (0.01–0.02 dex) for cluster results based on a single star, while the best covered clusters with 60 or more stars (Melotte 20 and Melotte 22) show an error of 0.05 dex. Metallicity spreads can be expected due to atomic diffusion for example (Souto et al. 2019).

The radial metallicity distribution of the different samples show a comparable behaviour, but the APOGEE data span a somewhat narrower metallicity range at the different galactocentric distances.

⁵ <http://github.com/jobovy/galpy> [version 1.6.0]

Table 3. Parameters of the most distant sample clusters.

Cluster	$\log t$	d (pc)	$E(B - V)$	source	Revised parameters			
					$\log t$	d (pc)	$E(B - V)$	[Fe/H]
Berkeley 18	9.64	5632	0.49	1	9.50	6310	0.55	-0.40
Berkeley 19	9.34	6568	0.27	1	9.40	5495	0.42	-0.30
Berkeley 20	9.76	8710	0.13	2	9.75	8710	0.17	-0.40
Berkeley 21	9.34	5012	0.78	2	9.30	6026	0.70	-0.30
Berkeley 22	9.38	5754	0.64	2	9.40	6918	0.63	-0.30
Berkeley 25	9.39	6780	0.35	1	9.60	7943	0.35	-0.25
Berkeley 29	9.57	13 183	0.12	2	9.60	13 183	0.09	-0.40
Berkeley 31	9.46	7586	0.19	2	9.45	7586	0.20	-0.40
Berkeley 33	8.37	5851	0.56	1	8.50	5754	0.61	-0.30
Berkeley 73	9.15	6158	0.22	1	9.20	7244	0.27	-0.20
Czernik 30	9.46	6647	0.20	1	9.40	7244	0.32	-0.40
IC 166	9.12	5285	0.80	1	9.10	5248	0.83	-0.10
King 2	9.61	6760	0.31	1	9.70	6607	0.40	-0.40
NGC 1798	9.22	5124	0.36	1	9.20	4571	0.47	-0.30
Saurer 1	9.70	13 183	0.14	3	9.70	13 183	0.17	-0.40
Tombaugh 2	9.20	7943	0.34	2	9.30	9120	0.30	-0.30

Notes. The sources of the initial parameters are as follows: (1) Cantat-Gaudin et al. (2020), (2) BOCCE, and (3) Carraro & Baume (2003). The last column lists the adopted metallicity for the corresponding isochrones.

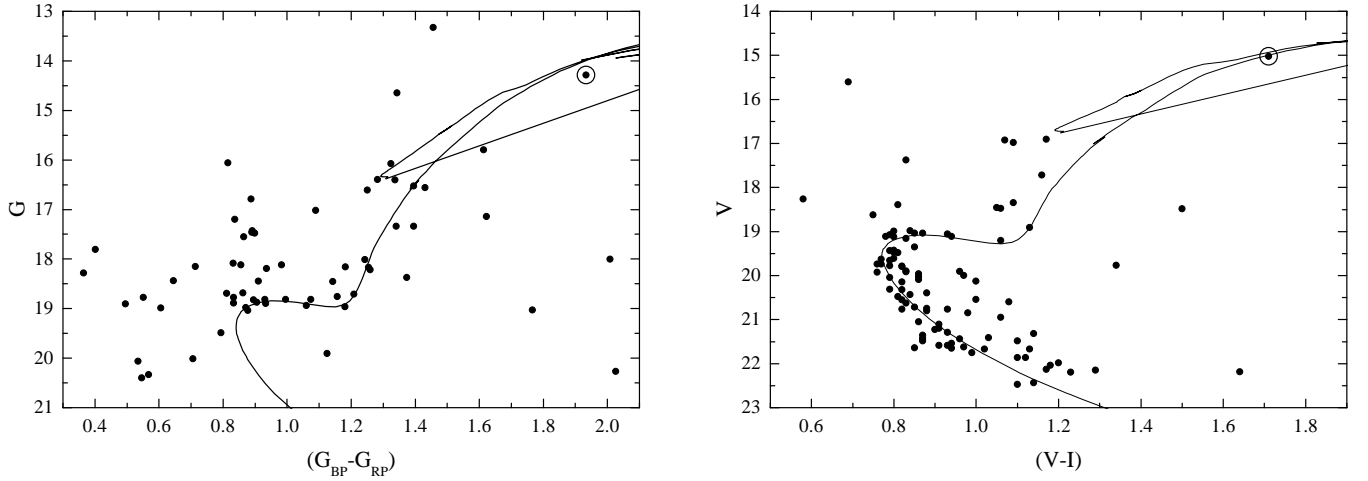


Figure 3. Result for the open cluster Saurer 1. The left-hand panel shows the *Gaia* CMD of proper motion members and the right-hand panel shows the *V I* data by Carraro & Baume (2003) restricted to the innermost cluster region. The overplotted isochrones correspond to the parameters listed in Table 3. The position of the star included in the spectroscopic study by Donor et al. (2020) is marked with a circle.

Table 4. Physical parameters of the 136 open clusters with spectroscopic metallicities – full table available as supplementary material at the CDS.

Cluster	l (deg)	b (deg)	$\log t$	Dist. (kpc)	[Fe/H] (deg)	σ [Fe/H] (deg)	No. stars / meas.	Source	R_{GC} (kpc)
NGC 6583	9.283	-2.534	9.08	2.05	0.37	0.04	2 / 2	2	5.99
NGC 6494	9.894	2.834	8.68	0.66	-0.04	0.08	3 / 6	2	7.35
Blanco 1	15.572	-79.261	7.98	0.24	0.04	0.07	6 / 6	2	7.96
Ruprecht 147	21.012	-12.816	9.48	0.32	0.12	0.03	27	1	7.71
NGC 6705	27.307	-2.776	8.40	2.09	0.12	0.04	12	1	6.22
...

Notes. The number of stars and measurements is given for the HQ and LQ samples. The source of the metallicity is as follows: (1) Donor et al. (2020); (2) HQ sample; (3) LQ sample.

Table 5. Orbital parameters of the 146 open cluster with spectroscopic and photometric metallicities – full table available as supplementary material at the CDS.

Cluster	RV (km s^{-1})	σRV (km s^{-1})	No. stars	R_{GC} (kpc)	R_{apo} (kpc)	R_{peri} (kpc)	R_{guide} (kpc)	ecc	z_{max} (kpc)
NGC 6583	-1.43	0.49	24	5.99	6.75	5.97	6.34	0.06	0.09
NGC 6494	-8.00	0.13	12	7.35	7.67	7.35	7.51	0.02	0.07
Blanco 1	6.23	0.07	172	7.96	8.49	7.96	8.16	0.03	0.22
Ruprecht 147	42.18	0.38	99	7.71	8.95	6.26	7.37	0.18	0.26
NGC 6705	34.49	0.27	357	6.22	6.53	5.51	5.98	0.08	0.09
...

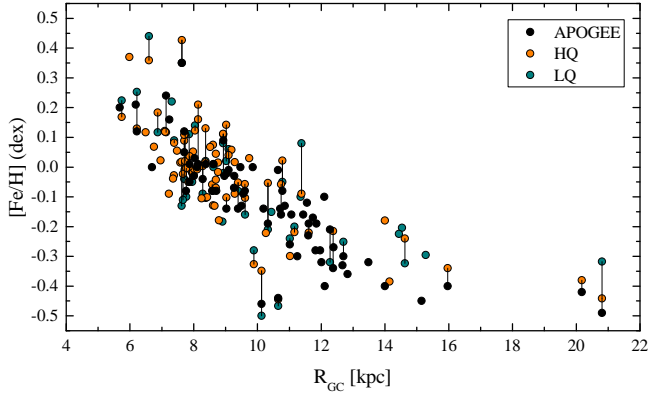


Figure 4. The galactic metallicity distribution based on open clusters with spectroscopic determinations. The connecting lines show objects in common in the three samples.

This might be related to the homogeneous analysis, but could be a bias due to the target sample as well, as several confirmed under- or overabundant objects are not covered by this survey.

In the following we merge the individual data sets to a single one by adopting APOGEE data as primary source, thus preferring homogeneity instead of spectral resolution, followed by 59 objects from the HQ compilation and seven clusters with LQ data. Figure 5 shows this merged sample in addition to the 11 objects analysed with the DG method that have no spectroscopic measurement available. The latter nicely match the spectroscopic distribution.

Previous works (see Netopil et al. 2016, and references therein) noticed a transition of the metallicity gradient between the inner and outer Galactic disc. While the inner disc shows a steeper gradient, the metallicity distribution of the outer area is almost flat. The above reference adopt $R_{GC} \sim 12$ kpc for this transition radius. More recently, Donor et al. (2020) used a two-line function fit to derive $R_{GC} \sim 13.9$ kpc, which however strongly depends on the adopted distance scale. Though the appearance of a “knee” in the metallicity distribution not only depends on the distance scale (note that the most distant objects were verified), also on the covered objects. Compared to Netopil et al. (2016) several outer disc clusters that led to a conclusion about a flat gradient are either much closer, more metal deficient or are even rejected (Berkeley 75, see Sect. 4.1) in the present data set. Furthermore, our data set includes nine additional objects more distant than $R_{GC} \sim 12$ kpc with spectroscopic metallicities and several photometrically analysed objects (Sect. 3.2) out to about $R_{GC} \sim 12$ kpc that provide a more clearer picture. At first glance, Fig. 5 does not indicate the existence of a gradient change, in

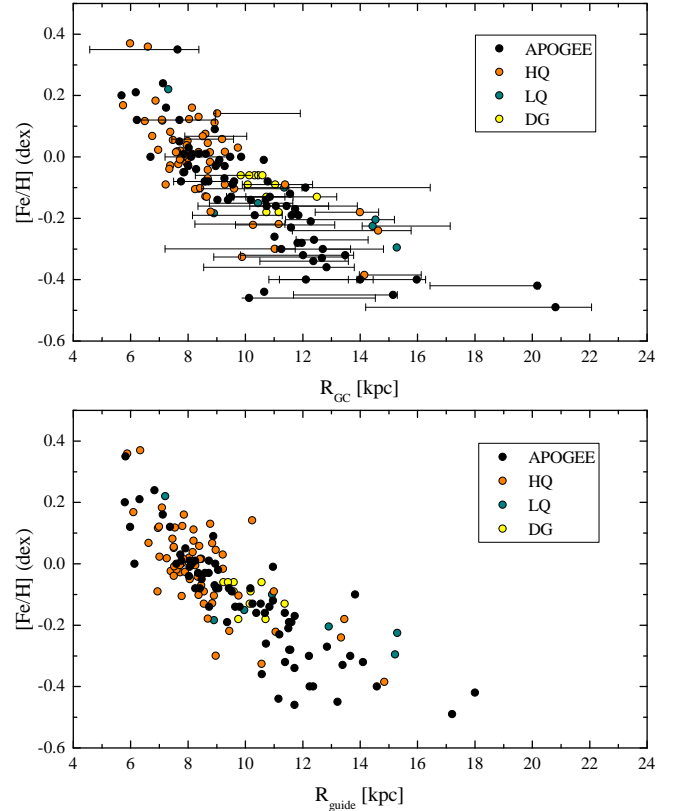


Figure 5. The galactic metallicity distribution based on the merged sample with spectroscopic determinations and the 11 objects presented in Sect. 3.2 without a spectroscopic measurement. The upper panel shows the distribution for R_{GC} , also the distance range of R_{apo} and R_{peri} for objects with orbit boundaries larger than 2 kpc is given. The lower panel presents the metallicity distribution for R_{guide} .

particular if the two most distant objects (Berkeley 29 and Saurer 1) are tuned out.

Using the total sample as presented in Fig. 5 (without the two objects mentioned above) and a linear regression model that is robust to outliers (Huber 1981) gives a gradient of $-0.058(4) \text{ dex kpc}^{-1}$. The clearly lowest weight was assigned to six objects, most of them already identified as “outliers” by Netopil et al. (2016): Melotte 66, NGC 2243, NGC 6253, NGC 6583, NGC 6791, and Trumpler 5. Repeating the analysis for inner disc objects only ($R_{GC} \leq 12$ kpc) results in a gradient of $-0.063(5) \text{ dex kpc}^{-1}$, the exclusion of the six deviating objects gives $-0.058(5) \text{ dex kpc}^{-1}$. We note, however, that

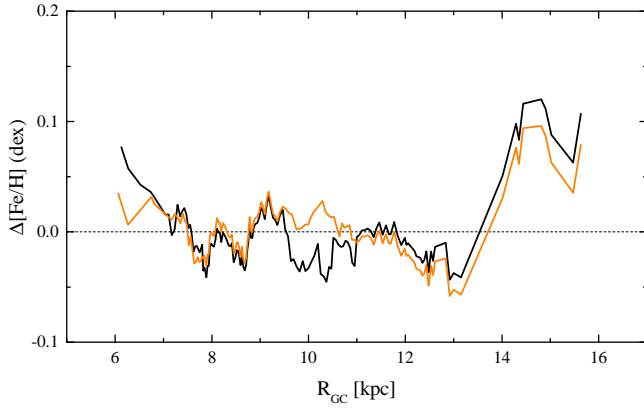


Figure 6. Residuals of the running average for the complete (black line) and cleaned sample (orange line) after subtracting the respective gradients of the inner disc objects.

the used regression model does only identifies possible outliers in the dependent variable.

For the identification of gradient changes, we use a running average on the residuals after subtraction of the gradients of inner disc objects. We grouped the sample either by a constant number of 15 clusters or by a maximum distance range of 1 kpc, whichever criterion was fulfilled first (see Netopil et al. 2016, for details). Figure 6 indicates that the gradient flattens slightly out beyond $R_{GC} \sim 13$ kpc, though to a much lower extent as shown e.g. by Netopil et al. (2016). However, the little coverage of objects beyond this region, the split in the metallicity distribution of HQ/LQ and APOGEE data (see Fig. 5), and the unequal distribution in age – most of them are older than ≥ 2 Gyr (see Fig. 7) – might result in an incorrect conclusion. Future studies, spectroscopically or even photometrically, are still needed to provide a better coverage of objects more distant than $R_{GC} \sim 13$ kpc.

5.2 Age dependence of the radial [Fe/H] gradient

An analysis of the overall metallicity gradient using the complete open cluster sample introduces a bias as one mixes populations with different ages. To obtain some idea about the time evolution of the metallicity gradient, one therefore has to restrict the sample to objects with comparable ages as already presented in several previous works (e.g. Carraro et al. 1998; Netopil et al. 2016; Donor et al. 2020, to mention just a few). Not only the number of available cluster data increased significantly since the work by Carraro et al. (1998) who used 37 objects in total, but certainly also the data quality the analysis is based on.

Our sample is large enough to divide it into age groups that still include a sufficient number of objects and span a wide range of galactocentric distances. We define eight consecutive and overlapping age groups to trace variations in more detail: < 0.4 a, $0.3 \leq a < 0.7$, $0.4 \leq a < 1.0$, $0.7 \leq a < 1.5$, $1.0 \leq a < 1.9$, $1.5 \leq a < 3.0$, $1.9 \leq a \leq 4.0$, and $3.0 \leq a \leq 5.2$ Gyr. The age groups are a reasonable compromise between the distributions in age and distance, number of objects, and covered age range. The six oldest open clusters are not considered in the analysis, because they will significantly enlarge the covered age range of the oldest age group, and are too small in number to represent an additional age group. Furthermore, we exclude the two most distant objects Berkeley 29 and Saurer 1 (see Fig. 5), because of their special Galactic location about 5 kpc more distant than other

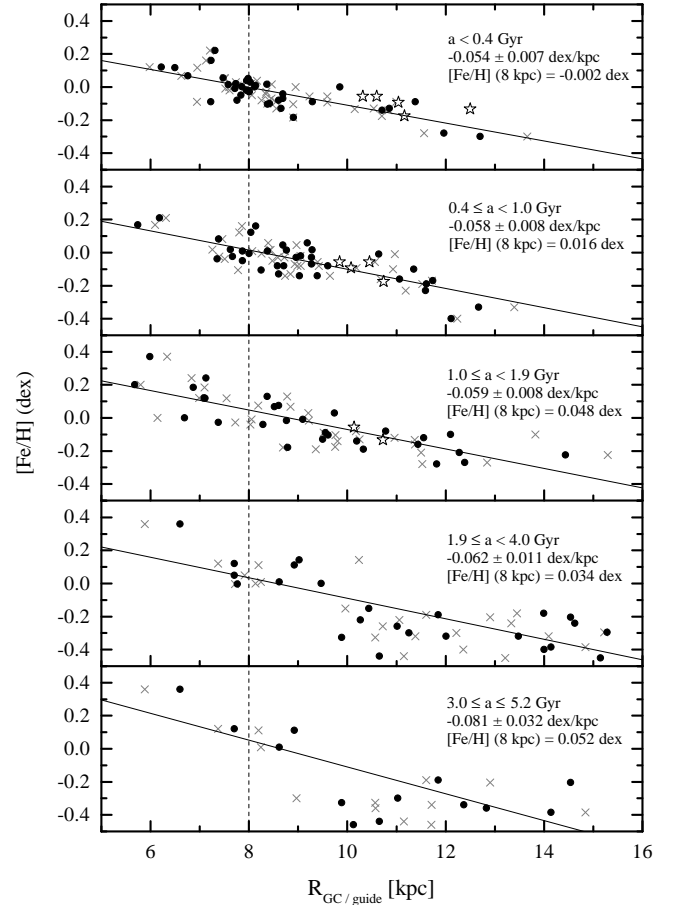


Figure 7. The metallicity distribution of five age groups. Overplotted are the derived gradients for R_{GC} using the robust fitting model. We also indicate their results and the metallicity levels at the solar circle. The photometric results are included as asterisks to show the good agreement with spectroscopic data. The R_{guide} positions are always given as crosses.

clusters in the sample. A short discussion of these objects is given in Sect. 5.4.

We derived the metallicity gradients of the age groups using a robust regression model (Huber 1981), already applied in Sect. 5.1, and a bootstrap method with 10 000 resampling iterations and linear least-squares regression. We note that the bootstrap distributions are almost Gaussian.

The results using R_{GC} as distance are listed in the upper panel of Table 6 and some age groups are shown in Fig. 7. All but the oldest group include about two to three dozens of objects and they cover distances out to about 13 kpc at least.

The results of the two approaches agree very well and indicate within the errors an almost constant metallicity gradient. The oldest age group (~ 4 Gyr), however, is showing a steeper gradient, but the errors and the small number of objects involved does not allow a firm conclusion. This result agrees very well with Casagrande et al. (2011) and Anders et al. (2017) for field stars. These indicate a flattening of the gradient only for older ages, which are not yet sufficiently covered by open clusters. Apart from the analysis of the defined age groups, we also performed a robust multiple linear regression on 130 clusters younger than about 3 Gyr by including also the age as

Table 6. Metallicity gradients of the age groups

Age (Gyr)	N	ZP	dex kpc ⁻¹	σ	ZP	dex kpc ⁻¹	σ
0.25 ± 0.11	41	0.43 ± 0.06	-0.054 ± 0.007	0.05	0.43 ± 0.06	-0.054 ± 0.007	0.06
0.45 ± 0.13	29	0.46 ± 0.09	-0.056 ± 0.009	0.07	0.47 ± 0.08	-0.057 ± 0.008	0.07
0.74 ± 0.18	39	0.48 ± 0.07	-0.058 ± 0.008	0.07	0.49 ± 0.08	-0.059 ± 0.008	0.07
0.98 ± 0.21	43	0.45 ± 0.07	-0.054 ± 0.008	0.09	0.50 ± 0.08	-0.059 ± 0.009	0.09
1.32 ± 0.29	31	0.52 ± 0.07	-0.059 ± 0.008	0.09	0.54 ± 0.09	-0.061 ± 0.008	0.09
2.00 ± 0.40	25	0.49 ± 0.09	-0.058 ± 0.008	0.09	0.49 ± 0.08	-0.058 ± 0.007	0.09
2.54 ± 0.69	24	0.53 ± 0.13	-0.062 ± 0.011	0.14	0.52 ± 0.13	-0.061 ± 0.011	0.14
3.98 ± 0.82	13	0.70 ± 0.35	-0.081 ± 0.032	0.18	0.63 ± 0.31	-0.076 ± 0.028	0.18
0.25 ± 0.11	41	0.44 ± 0.05	-0.057 ± 0.006	0.06	0.46 ± 0.06	-0.058 ± 0.007	0.06
0.45 ± 0.13	29	0.44 ± 0.05	-0.056 ± 0.006	0.05	0.47 ± 0.06	-0.058 ± 0.006	0.05
0.74 ± 0.18	38	0.52 ± 0.07	-0.063 ± 0.008	0.07	0.52 ± 0.08	-0.063 ± 0.008	0.07
0.98 ± 0.21	42	0.50 ± 0.08	-0.059 ± 0.009	0.09	0.51 ± 0.11	-0.059 ± 0.012	0.09
1.32 ± 0.29	31	0.47 ± 0.09	-0.055 ± 0.010	0.10	0.48 ± 0.11	-0.055 ± 0.011	0.10
2.00 ± 0.40	25	0.43 ± 0.10	-0.054 ± 0.009	0.10	0.44 ± 0.09	-0.055 ± 0.009	0.10
2.54 ± 0.69	24	0.57 ± 0.12	-0.067 ± 0.011	0.12	0.57 ± 0.11	-0.067 ± 0.010	0.12
3.98 ± 0.82	13	0.67 ± 0.20	-0.084 ± 0.019	0.15	0.68 ± 0.25	-0.083 ± 0.024	0.15

Notes. The left-hand side represents the results based on robust regression, and the right-hand side the results using a bootstrap method. The upper panel provides the gradients based on R_{GC} and the lower one using R_{guide} . The median age of each group is given in the first column, also the number of objects (N) and the chemical dispersion in each age group (σ) is listed. We note that we were not able to derive R_{guide} for one object (Berkeley 104) that is included in age groups 3 and 4.

independent variable (the errors of the last significant digits are given in parenthesis):

$$[Fe/H] = 0.49(4) - 0.060(4) R_{GC} + 0.020(10) \text{ Gyr} (\sigma = 0.08 \text{ dex}). \quad (3)$$

Netopil et al. (2016) list gradients for two analysed age groups that are considerable larger than ours. This is a result of a much narrower covered R_{GC} range where inaccurate data have a stronger influence on the derived gradient, the inclusion of some cluster metallicities that are actually based on non-members (see Sect. 4.1), but also based on differences in the adopted cluster age and distance. Netopil et al. (2016) use mean literature results, which generally reduces the influence of inaccurate parameters. However, this approach is probably not suited for little studied objects. One example is NGC 2354, for which a mean age of about 0.2 Gyr and a distance of 3.6 kpc is listed. However, the adopted results by Cantat-Gaudin et al. (2020) quote about 1.4 Gyr and 1.4 kpc based on *Gaia* data. We inspected the *Gaia* CMD and conclude that Cantat-Gaudin et al. (2020) provide a reasonable parametrization for this object. This clearly shows the advantage of the availability of *Gaia* photometric and astrometric data for open cluster research, in particular to identify true giant star members to better constrain the age.

The shallower gradients that we derive for the youngest age groups agree very well with results based on Cepheid stars (Genovali et al. 2014), who derived -0.051 to -0.06 dex kpc⁻¹ using different samples. Anders et al. (2017), on the other hand, used red giant stars to derive -0.058 dex kpc⁻¹ (their bias-corrected result) for the youngest group (< 1 Gyr).

A step-like discontinuity of the metallicity gradient as proposed by Lépine et al. (2011) can be generally ruled out for the youngest age groups. For the older groups, however, one might identify such a jump of the metallicity level. Though this appearance is very probably just caused by the lower number of objects and the stronger influence of migration effects in these groups, which cover a much larger age range. Resonances have certainly an impact on the clusters' distribution as shown by Monteiro et al. (2021), but these effects

must be observed more clearer among the youngest objects that have not moved much from their birth places.

Baratella et al. (2020) presented a new approach to derive abundances for young dwarf stars in open clusters. They noticed that the microturbulence parameter is overestimated if using a “standard” analysis, resulting in an underestimate of the metal content. The largest differences were found for clusters younger than 100 Myr. We note that their results are not included in our sample, though all their objects, except NGC 2547, for which we derive an offset of about 0.1 dex. Thus, the result for our youngest cluster population might be affected. However, our youngest group includes only eight objects that are younger than 100 Myr and 12 objects in total with a metallicity that is based on dwarf stars. Even the exclusion of all objects younger than 150 Myr results in a gradient of -0.054 dex kpc⁻¹ and a metallicity level at the solar circle of -0.012 dex for the youngest age group, in agreement to the results listed in Table 6 and shown in Fig. 7. The median age of the remaining objects is only slightly increased to 280 Myr.

Recently, Spina et al. (2021) used combined GALAH (Buder et al. 2021) and APOGEE data for a study of the metallicity gradients. They used 134 open clusters, a sample of similar size to ours. However, except one object all of them are closer than $R_{GC} \sim 13$ kpc (adopting $R_{\odot} \sim 8.2$ kpc). They conclude that the guiding radius R_{guide} is a better distance indicator for metallicity gradient analyses and reduces effects by blurring. We therefore repeated the previous calculations using R_{guide} instead of R_{GC} . Although the use of R_{guide} provides a smoother metallicity distribution for some “outliers”, some others pop up as new deviating objects. The results in the lower panel of Table 6 show that the gradients do not differ significantly, these agree very well within the errors. The chemical dispersion does not significantly improve as well, except in the very oldest group, in some age groups the use of R_{guide} even results in marginal larger dispersions.

Furthermore, a multiple linear regression provides almost the same result as for R_{GC} :

$$[Fe/H] = 0.49(3) - 0.061(4) R_{guide} + 0.018(9) \text{ Gyr} (\sigma = 0.07 \text{ dex}). \quad (4)$$

From fig. 7 by Spina et al. (2021), we infer that the metallicity gradient of their second age group (1–2 Gyr) does not change, while the others show shallower gradient by $0.02 - 0.06 \text{ dex kpc}^{-1}$ using R_{guide} as distance indicator. In contrast, the overall gradient remain almost the same using R_{GC} ($-0.076 \text{ dex kpc}^{-1}$) or R_{guide} (-0.073 dex/kpc). This generally can be explained if one group shows a better distance range covering or contributes most to the complete sample. Furthermore, for the youngest groups, one would expect the least influence by blurring (see e.g. Tarricq et al. 2021), which is also supported by the results in Table 6. The differences between our study and Spina et al. (2021) might be related with their broad age groups or insufficient distance coverage in the individual age groups, but the main difference is the adopted distance scale. Spina et al. (2021) used *Gaia* parallax data to infer the cluster distances. These are certainly useful for closer objects, but the distances of objects more distant than $\sim 3 \text{ kpc}$ are continuously underestimated – Berkeley 20 and Berkeley 29 even by more than 4 kpc compared to our scale. This certainly produces steeper metallicity gradients using R_{GC} , but it is out of scope to evaluate the influence of the underestimated distances on R_{guide} . Thus, a comparison of metallicity gradients from different studies is complicated by the use of different distance scales, but also by the covered range of galactocentric distances and the applied method to derive the gradients.

5.3 Radial migration

Radial migration is already a well-known effect, but it is still not well understood. Available chemodynamical models significantly differ in their approach: e.g. Schönrich & Binney (2009) introduced a parametrization by hand, while Minchev et al. (2013) used a cosmological simulation. However, radial migration appears important even for older kinematic hot populations.

An increase of the metallicity level at the solar circle with age can be noticed in several open cluster studies (e.g. Jacobson et al. 2016; Netopil et al. 2016; Donor et al. 2020; Spina et al. 2021). Netopil et al. (2016) conclude that this metallicity shift might be related with radial mixing. This behaviour seems independent on the used data and is also clearly present in our study. The derived metallicity gradients indicate a constant increase of the metallicity level at the solar circle for clusters up to about 2 Gyr (see Fig. 7). This is supported by the results of the multiple linear regressions in Sect. 5.2; thus, it is not artificially caused by a possible inappropriate grouping. The simulation by Anders et al. (2017) shows that radial mixing might produce a metallicity shift of about $+0.1 \text{ dex}$ after $\geq 2 \text{ Gyr}$ by bringing metal-rich objects from inner regions to the solar circle. This metallicity increase is obviously about twice as large than supported by our data, though one has to keep in mind that the metallicity gradient and metallicity level of the ISM has changed in the past. Fig. 5 by Minchev et al. (2018) indicates that the metallicity level at the solar circle was about 0.1 dex lower 3 Gyr ago and the gradient about $0.01 \text{ dex kpc}^{-1}$ steeper 4 Gyr ago.

We adopt the model by Minchev et al. (2018) and used our youngest age group as a basis for the current ISM to estimate the birth radii (R_{birth}). For the youngest age group one can assume that these clusters have not moved much since birth, but erroneous metallicities might still alter the derived gradients. We therefore checked the results by excluding few objects that show the lowest weight (< 0.7) in the

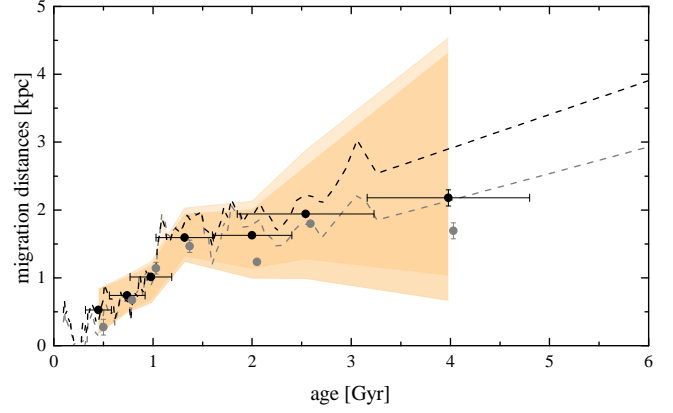


Figure 8. The required mean movement of the clusters by migration as a function of age. We provide the mean value derived from the two gradient sets (robust fitting and bootstrap method). The inner area shows the error range by considering the uncertainty of the regression analysis, the outer area includes also the error in age. The youngest age group was omitted as it deals as the reference for the present ISM. The dashed lines represent the running average on the individual migration distances. The black symbols and line represent the migration distance $R_{GC} - R_{birth}$, the grey ones $R_{guide} - R_{birth}$.

robust fitting procedure. This removed five and four clusters from the R_{GC}/R_{guide} samples, respectively. The clearly lowest weight (< 0.4) was assigned to NGC 6087 in both samples. The cleaned data sets provide in both cases a gradient of $-0.055(5) \text{ dex kpc}^{-1}$ in good agreement with the results in Table 6. We note that for older age groups, which are probably already affected by radial migration, such a procedure could be problematic as it also might reduce the scatter caused by radial migration.

We finally derive the migration distances $R_{GC} - R_{birth}$ and $R_{guide} - R_{birth}$ in two ways, first using the gradients of the individual age groups (adopting the solar circle as reference point), but also for all individual objects. However, we note that it is impossible to derive the true birthplaces as one has to assume that the ISM gradient has zero scatter.

Figure 8 shows the required mean movement by migration from the inner disc as a function of age by considering the present-day metallicity levels and gradients of each mono-age population and the changes of the ISM metallicity level and gradient in the past. We derived the migration distances using the two gradient sets (obtained by robust fitting and the bootstrap method), which agree very well. Furthermore, we present a running average of the migration distances derived for the individual objects. Here we use a grouping of 15 open clusters up to an age of 4 Gyr, the remaining 11 oldest objects represent a separate group. We present the results using the two distance indicators R_{GC} and R_{guide} . Whereas the first provides an estimate of the total radial mixing by churning and blurring, R_{guide} gives an indication for churning only.

For clusters younger than about 1.5 Gyr we notice a mean migration rate of 1 kpc Gyr^{-1} . This agrees with a radial migration model (Quillen et al. 2018) based on shearing sheet N -body simulations, which is suitable for younger objects up to about 1 Gyr (or about five orbital periods). They quote a maximum migration rate of 1 kpc Gyr^{-1} for a pitch angle of 24° , which shows a good agreement with our results for the youngest clusters. However, they note that this migration rate is probably underestimated, because they derived higher rates for some open clusters. Our results probably include some underestimate as well. Recently, Sysoliatina & Just

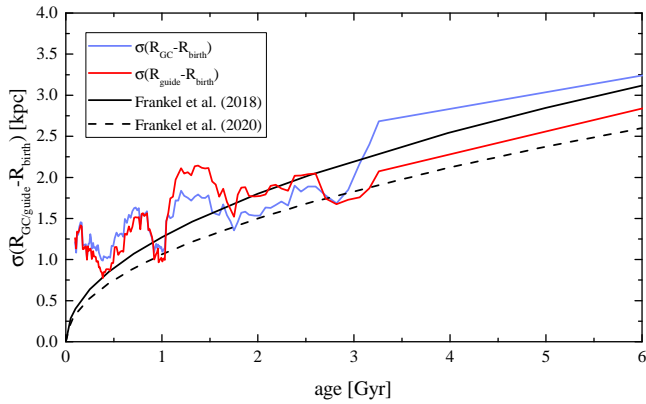


Figure 9. The evolution of the scatter, derived for R_{GC} and R_{guide} , compared with the radial migration efficiency models by Frankel et al. (2018, 2020).

(2021) identified a star formation burst about 0.5 Gyr ago. Assuming that this burst increased the overall metallicity level of subsequent generations, thus in particular of our youngest age group that was used as a reference, our calculations start from a somewhat too high metallicity level.

For older clusters different conclusions might be drawn from the results of the two analysis methods. The results of the gradient analysis would indicate that clusters almost do not migrate after 1.5 Gyr and that the little additional migration distances are just caused by blurring effects. This conclusion, however, rests on the oldest age group at 4 Gyr, which shows quite large errors for the gradient fits. A marginally flatter gradient would bring the migration distance already in line with the results obtained from the individual objects. These data on the other hand suggest that for older (2–6 Gyr), dynamically hotter, populations the total mean migration rate drops to $\sim 0.5 \text{ kpc Gyr}^{-1}$ with a contribution by churning of 0.3 kpc Gyr^{-1} . Furthermore, at an age of 6 Gyr, blurring already adds about 1 kpc to the total migration distance. This is compatible with a model by Frankel et al. (2020), which suggests a radial epicycle spread of about 1.3 kpc after 6 Gyr. There are some limitations in these findings as well, because first it does not account for possible differences with the galactic location. Actually, the mean galactocentric distance increases constantly with age from 8 to 12 kpc. Furthermore, the scatter of the migration distances is of the same order as the mean values.

However, the evolution of the scatter provides a useful information as well. The radial migration efficiency models were fitted to red clump star data by Frankel et al. (2018, 2020) to retrace their chemical dispersion with age. Their earlier model is purely spatial and does not include the dynamics (see Frankel et al. 2020). The difference in the models thus represents the influence by blurring. Figure 9 shows the evolution of the scatter in our data and compares it with the two models above. These generally follow the trend in our data; also, the increase of the scatter by blurring is well reproduced at least for an age $> 3 \text{ Gyr}$. This agrees with the findings in Table 6, where the two oldest groups show a noticeable reduction of the scatter between R_{GC} and R_{guide} .

A comparable approach to ours was adopted by Chen & Zhao (2020). They used the sample by Netopil et al. (2016) including also their photometric data compilation, which contributes about 40 per cent to the total sample. They note that blurring causes significant radial excursions for only 10 per cent of the clusters, which are mainly located in outer Galactic regions. Furthermore, they found that among the migrating objects younger clusters ($< 1 \text{ Gyr}$) tend to

migrate inwards while older ones migrate outwards. The photometric sample by Netopil et al. (2016) without any spectroscopic data covers mostly younger objects (~ 70 per cent $< 0.5 \text{ Gyr}$) close to the solar circle. For the majority of these objects also only a single photometric metallicity estimate from various methods is available and their reliability was questioned by Netopil et al. (2016). We therefore conclude that in particular the conclusion by Chen & Zhao (2020) for their young group is probably strongly biased by photometric data.

Zhang et al. (2021) on the other hand compiled only spectroscopic data and conclude that 46 per cent of open clusters migrated more than 1 kpc and that older clusters generally migrate outward. In agreement with our finding, they derived a migration rate of about 1 kpc/Gyr for the youngest clusters. Furthermore, using their criterion for migrators, we derive an almost identical value of 51 per cent.

Considering the uncertainty introduced by the ISM model in our calculations and the limitation by using a 0.25-Gyr-old population as a proxy for the current ISM, we conclude that the observed increase of the metallicity levels with age can be quite well explained by radial migration itself. There is actually no need to introduce other explanations as main solution for a lower metallicity level of young clusters, such as systematics in the spectroscopic analysis due to stellar activity, for example. Using for example the models by Minchev et al. (2018) and Quillen et al. (2018), one must observe some increase of the metallicity level, because the resulting shift in the metallicity is about a factor of 2 larger than the decreasing one with age of the ISM model. In other words, a decrease of the metallicity levels with age might be only noticed if the radial migration efficiency is lower than about 0.5 kpc/Gyr.

Anders et al. (2017) proposed a mechanism including radial mixing and a more prone tidal disruption of inward-migrating objects to explain observed discrepancies between the gradient evolution of clusters and field stars. In our sample we notice only 12 inward-migrating objects (most of them younger than 1 Gyr) using $(R_{guide} - R_{birth}) < -1 \text{ kpc}$, and 49 per cent probable non-migrators using $|R_{guide} - R_{birth}| < 1 \text{ kpc}$. The low number of inward-migrating objects might support their proposal. However, our results for the gradients (Table 6) are quite constant over time and reasonably agree with results for field stars (Casagrande et al. 2011; Genovali et al. 2014; Anders et al. 2017). An exception is the oldest age group (4 Gyr), for which we still find a somewhat steeper gradient, but the low number of covered objects and the large error of the gradient does still not allow a firm conclusion for this age range – see e.g. also the discussion by Anders et al. (2017) for their little covered oldest age group ($> 10 \text{ Gyr}$). On the other hand, the evolution of the scatter of the migration distances (Fig. 9) agrees very well with the results by Frankel et al. (2018, 2020), suggesting that there might be no peculiarity of the open cluster population. Future studies are clearly needed to improve the coverage of the oldest open clusters.

5.4 Objects of special interest

The current Galactic position of the most distant open clusters in our sample (Berkeley 29 and Saurer 1) does absolutely not fit to the radial metallicity distribution of the other clusters with a comparable age. Their orbits span a wide range in distance (see Fig. 5) and only their pericentre radii (or very close to them) would agree with the other clusters' metallicity distribution. Furthermore, their current position above the Galactic plane ($> 1.5 \text{ kpc}$) is close to their orbital boundary value z_{max} . Carraro & Bensby (2009) speculated about an extragalactic origin of these objects, Cantat-Gaudin et al. (2016), on the other hand, note that the mean abundances place them at the

limit between the α -rich thin disc and the α -poor thick disc without strong evidence of an extragalactic origin, but their orbits might be perturbed by accretion events or minor mergers in the past. In case of the last, it will be challenging to conclude about their actual birth radii.

In the following, we discuss deviating objects using the weight of the applied robust fitting method as indicator. Figure 5 shows three objects with an apparent metal deficiency compared to other clusters at the same distance ($R_{GC} \sim 10$ kpc): NGC 2243, Melotte 66, and Trumpler 5 (age ~ 4 -5 Gyr). These were identified as deviating objects in Sect. 5.1, and two of them (NGC 2243 and Trumpler 5) also in the analysis of the age dependence of the radial [Fe/H] gradient (Sect. 5.2). For all three clusters, their apocentre radii are in better agreement with the radial metallicity distribution of other objects in their age group. For two about 0.7-Gyr-old objects (NGC 2632 and FSR 716), an eccentric orbit already might explain their deviation, but for NGC 6087 and NGC 6583 there might be some issue concerning age, distance, metallicity scale, or they show a quite different radial migration efficiency.

A check of the *Gaia* CMDs does not show noticeable problems with their adopted distance and age. The about 100-Myr-old cluster NGC 6087 is only included in the very youngest age group, suggesting that an unsuitable age group is very probably not the reason for the deviation. However, the adopted LQ metallicity of 0.22 dex is based on a single (Cepheid) star measured by Luck (1994). An additional literature search noticed a newer result for the star by this author (Luck 2018) with a lower metallicity: 0.11 dex. Furthermore, a photometric estimate of the cluster using the DG method gives 0.04 dex (Netopil et al. 2016).

The metal-rich open cluster NGC 6583, on the other hand, deviates in two overlapping age groups. Quillen et al. (2018) conclude for this about 1.2-Gyr-old inner disc open cluster, currently located at $R_{GC} \sim 6$ kpc, that either the Milky Way bar ejected the object from the inner Galaxy or a radial migration of 2-3 kpc/Gyr is required to explain the current position. This estimate is about a factor of 2-3 larger than the mean radial migration we found for objects of comparable age. We estimate for this cluster even a much larger migration distance of about 5 kpc.

Another metal-rich inner disc cluster, mentioned as a special case in several previous studies, is NGC 6791. It is not included in our investigation of the age dependence of the radial [Fe/H] gradient because of the little number of very old objects in the sample. With an age of about 8.5 Gyr, it even belongs to the very oldest open clusters known in the Galaxy (see e.g. the catalogue by Cantat-Gaudin et al. 2020). This cluster shows the most eccentric orbit in our sample with a pericentre distance of $R_{GC} \sim 4.6$ kpc (see Figure 5). Furthermore, due to its age, also the largest migration distance by churning was estimated (almost 7 kpc). Thus, suggesting a birthplace close to the Galactic Centre as for NGC 6583, if their metallicity is correct.

6 SUMMARY AND CONCLUDING REMARKS

This work presents a combined data set of spectroscopic metallicities for 136 open clusters in total. The cluster membership of a part of the sample, which was compiled in the pre-*Gaia* era, was verified, resulting in the exclusion of some open cluster results that probably influenced previous conclusions based on these data. The other important fundamental cluster parameters (distance and age) were evaluated in particular for the most distant objects in the sample to

reduce the influence of inaccurate distances on the analysis of the metallicity gradients.

Furthermore, we present a complete parametrization of 14 open cluster using a photometric method. These objects are located in a somewhat outer Galactic region ($R_{GC} \sim 10$ -12 kpc) to improve the coverage of objects in this region. A good agreement with spectroscopic data was noticed, suggesting that the photometric approach provides a solid basis for future extensions. For example, we still notice a lack of a suitable coverage of metallicity among the oldest open clusters and in the outer disc. The total sample includes only about 20 objects older than 3 Gyr and only a dozen clusters more distant than 13 kpc from the Galactic Centre.

The data were used to investigate the radial metallicity distribution, the age dependence of the radial [Fe/H] gradient using mono-age populations of eight consecutive and overlapping age groups using objects up to about 5 Gyr, and to study the radial migration efficiency. Furthermore, we discuss some special objects of interest, which apparently do not follow the general trend in the metallicity distributions.

We do not notice a significant change of the metallicity gradient out to $R_{GC} \sim 13$ kpc. A somewhat shallower gradient might be present beyond this radius, but the small number of covered objects in this Galactic region does not allow a firm conclusion yet. Though, based on the oldest clusters only one might conclude a flattening of the gradient already at about 10 kpc in agreement with Monteiro et al. (2021). However, the much smaller number of older objects requires the use of larger age ranges to define suitable covered mono-age populations, resulting in a larger scatter probably caused by radial migration effects. Thus, the metal content of more old clusters is needed to better pinpoint the trend and evolution of their metallicity gradients.

The analysis of the age groups shows almost constant gradients, somewhat steeper gradients are noticed only for the oldest clusters, which however are little covered. Furthermore, we notice increasing metallicity levels with age, which we interpret as a result of a radial outward migration rate of 1 kpc/Gyr for objects younger than ~ 2 Gyr. For older objects the results differ between the adopted methods (analysis of the gradients and using mean migration distances of the individual objects). The metallicity gradients indicate little additional migration, a conclusion very probably caused by the insufficiently covered oldest age group; the analysis of the individual objects, however, provides a total migration rate of about 0.5 kpc/Gyr between 2 and 6 Gyr, with churning somewhat stronger than blurring. The use of R_{GC} and R_{guide} as distance proxy indicates that the epicyclic excursions start to be recognisable after 2 Gyr and contribute about 1 kpc to the total migration distance after 6 Gyr. A comparison of our migration distance estimates, but also their scatter, with radial migration models, shows good agreement.

We still have to deal with an observational bias in the metallicity distribution. Most of the outer disc objects ($R_{GC} \gtrsim 13$ kpc) with known metallicity are older than about 2 Gyr. These are certainly easier to identify and to investigate because of their outlying position from the Galactic plane. Furthermore, the use of red giants are preferred in spectroscopic studies. Young distant objects are more obscured and are generally little known, the catalogue by Cantat-Gaudin et al. (2020) only includes 24 objects younger than 1 Gyr with a distance of $R_{GC} > 13$ kpc. In the solar neighbourhood, however, the age distribution shows that the younger ones represent the by far most frequent population (Anders et al. 2021).

With increasing sample sizes one certainly also has to deal with an increasing number of objects that apparently do not fit into the overall picture. This might be simply related to inaccurate data, be-

cause most open cluster metallicities are based on few or even on a single star, or to specific peculiarities of the cluster. For some objects such as Berkeley 29 and Saurer 1, the most distant clusters in our sample, their orbit boundaries might explain their outstanding position in the metallicity distribution. For two clusters (NGC 6583 and NGC 6791), the known metallicity suggests a birthplace close to the Galactic Centre. For the much younger one (NGC 6583, 1.2 Gyr), this already implies a migration rate of about 4 Gyr/kpc. At least for one object (NGC 6087), the metallicity scale definitely requires further verification.

That *Gaia* data have already significantly improved numerous topics in Galactic research is beyond doubt. Future data releases will also include homogeneous astrophysical parameters based on the full BP and RP spectrophotometry and even more precise using data from the higher resolution radial velocity spectrograph. In combination with future individual spectroscopic or photometric studies, and ongoing or future large-scale spectroscopic surveys, the better sampling will also allow to switch from analyses using simple linear regressions to well-covered segmentations, to study regional properties of mono-age populations in even more detail.

ACKNOWLEDGEMENTS

We thank the referee, Friedrich Anders, for valuable comments to improve this paper. MN would also like to thank Barbara, Axel, and Erik for their patience during preparation of this paper. This paper is based upon observations carried out at the Observatorio Astronómico Nacional on the Sierra San Pedro Mártir (OAN-SPM), Baja California, México. This paper has also made use of results from the European Space Agency (ESA) space mission *Gaia*, the data from which were processed by the *Gaia* Data Processing and Analysis Consortium (DPAC). Funding for the DPAC has been provided by national institutions, in particular the institutions participating in the *Gaia* Multilateral Agreement. The *Gaia* mission website is <http://www.cosmos.esa.int/gaia>. Furthermore, this research has made use of the WEBDA data base (<https://webda.physics.muni.cz>), operated at the Department of Theoretical Physics and Astrophysics of the Masaryk University.

DATA AVAILABILITY

The data underlying this paper are available at the CDS. These cover the complete Tables 4 and 5, and the derived differential grids.

REFERENCES

- Akkaya Oralhan I., Schuster W. J., Michel R., Chavarría-K. C., Moitinho A., Vázquez R., Karataş Y., 2010, *Rev. Mex. Astron. Astrofis.*, **46**, 385
- Akkaya Oralhan I., Karataş Y., Schuster W. J., Michel R., Chavarría C., 2015, *New Astron.*, **34**, 195
- Akkaya Oralhan I., Michel R., Schuster W. J., Karataş Y., Karsli Y., Chavarría C., 2019, *Journal of Astrophysics and Astronomy*, **40**, 33
- Akkaya Oralhan I., Michel R., Karsli Y., Çakmak H., Sung H., Karataş Y., 2020, *Astronomische Nachrichten*, **341**, 44
- Alonso A., Arribas S., Martínez-Roger C., 1996, *A&A*, **313**, 873
- Anders F., et al., 2017, *A&A*, **600**, A70
- Anders F., Cantat-Gaudin T., Quadrino-Lodoso I., Gieles M., Jordi C., Castro-Ginard A., Balaguer-Núñez L., 2021, *A&A*, **645**, L2
- Balaguer-Núñez L., Tian K. P., Zhao J. L., 1998, *A&AS*, **133**, 387
- Bartella M., et al., 2020, *A&A*, **634**, A34
- Bessell M. S., Castelli F., Plez B., 1998, *A&A*, **333**, 231
- Bossini D., et al., 2019, *A&A*, **623**, A108
- Bovy J., 2015, *ApJS*, **216**, 29
- Bragaglia A., Tosi M., 2006, *AJ*, **131**, 1544
- Bressan A., Marigo P., Girardi L., Salasnich B., Dal Cero C., Rubele S., Nanni A., 2012, *MNRAS*, **427**, 127
- Brunthaler A., et al., 2011, *Astronomische Nachrichten*, **332**, 461
- Buder S., et al., 2021, *MNRAS*, **506**, 150
- Cantat-Gaudin T., Anders F., 2020, *A&A*, **633**, A99
- Cantat-Gaudin T., Donati P., Vallenari A., Sordo R., Bragaglia A., Magrini L., 2016, *A&A*, **588**, A120
- Cantat-Gaudin T., et al., 2020, *A&A*, **640**, A1
- Carraro G., Baume G., 2003, *MNRAS*, **346**, 18
- Carraro G., Bensby T., 2009, *MNRAS*, **397**, L106
- Carraro G., Ng Y. K., Portinari L., 1998, *MNRAS*, **296**, 1045
- Carrera R., et al., 2019, *A&A*, **623**, A80
- Casagrande L., Schönrich R., Asplund M., Cassisi S., Ramírez I., Meléndez J., Bensby T., Feltzing S., 2011, *A&A*, **530**, A138
- Casamiquela L., et al., 2017, *MNRAS*, **470**, 4363
- Chen Y. Q., Zhao G., 2020, *MNRAS*, **495**, 2673
- Dias W. S., Monteiro H., Lépine J. R. D., Prates R., Gneiding C. D., Sacchi M., 2018, *MNRAS*, **481**, 3887
- Donor J., et al., 2020, *AJ*, **159**, 199
- Evans D. W., et al., 2018, *A&A*, **616**, A4
- Flower P. J., 1996, *ApJ*, **469**, 355
- Frankel N., Rix H.-W., Ting Y.-S., Ness M., Hogg D. W., 2018, *ApJ*, **865**, 96
- Frankel N., Sanders J., Ting Y.-S., Rix H.-W., 2020, *ApJ*, **896**, 15
- Gaia* Collaboration et al., 2018a, *A&A*, **616**, A1
- Gaia* Collaboration et al., 2018b, *A&A*, **616**, A10
- Genovali K., et al., 2014, *A&A*, **566**, A37
- Huber P. J., 1981, *Robust statistics*
- Jacobson H. R., Pilachowski C. A., Friel E. D., 2011, *AJ*, **142**, 59
- Jacobson H. R., et al., 2016, *A&A*, **591**, A37
- Janes K. A., 1979, *ApJS*, **39**, 135
- Jönsson H., et al., 2020, *AJ*, **160**, 120
- Landolt A. U., 2009, *AJ*, **137**, 4186
- Lépine J. R. D., et al., 2011, *MNRAS*, **417**, 698
- Lucas P. W., et al., 2008, *MNRAS*, **391**, 136
- Luck R. E., 1994, *ApJS*, **91**, 309
- Luck R. E., 2018, *AJ*, **156**, 171
- Magrini L., et al., 2017, *A&A*, **603**, A2
- Minchev I., Chiappini C., Martig M., 2013, *A&A*, **558**, A9
- Minchev I., et al., 2018, *MNRAS*, **481**, 1645
- Monteiro H., Barros D. A., Dias W. S., Lépine J. R. D., 2021, *Frontiers in Astronomy and Space Sciences*, **8**, 62
- Netopil M., Paunzen E., 2013, *A&A*, **557**, A10
- Netopil M., Paunzen E., Carraro G., 2015, *A&A*, **582**, A19
- Netopil M., Paunzen E., Heiter U., Soubiran C., 2016, *A&A*, **585**, A150
- Pecaut M. J., Mamajek E. E., 2013, *ApJS*, **208**, 9
- Pedregosa F., et al., 2011, *Journal of Machine Learning Research*, **12**, 2825
- Pöhl H., Paunzen E., 2010, *A&A*, **514**, A81
- Quillen A. C., Nolting E., Minchev I., De Silva G., Chiappini C., 2018, *MNRAS*, **475**, 4450
- Sariya D. P., Yadav R. K. S., Bellini A., 2012, *A&A*, **543**, A87
- Schönrich R., Binney J., 2009, *MNRAS*, **396**, 203
- Schönrich R., Binney J., Dehnen W., 2010, *MNRAS*, **403**, 1829
- Schuster W., et al., 2007, in Combes F., Palouš J., eds, Vol. 235, *Galaxy Evolution across the Hubble Time*. pp 331–331, doi:10.1017/S1743921306010039
- Sellwood J. A., Binney J. J., 2002, *MNRAS*, **336**, 785
- Skrutskie M. F., et al., 2006, *AJ*, **131**, 1163
- Souto D., et al., 2019, *ApJ*, **874**, 97
- Spina L., et al., 2021, *MNRAS*, **503**, 3279
- Stetson P. B., 1987, *PASP*, **99**, 191
- Sysoliatina K., Just A., 2021, *A&A*, **647**, A39
- Tapia M. T., Schuster W. J., Michel R., C. Chavarría-K. Dias W. S., Vázquez R., Moitinho A., 2010, *MNRAS*, **401**, 621
- Tarricq Y., et al., 2021, *A&A*, **647**, A19

- Tosi M., Di Fabrizio L., Bragaglia A., Carusillo P. A., Marconi G., 2004, [MNRAS](#), **354**, 225
- Wu Z. Y., Tian K. P., Balaguer-Núñez L., Jordi C., Zhao L., Guibert J., 2002, [A&A](#), **381**, 464
- Zhang H., Chen Y., Zhao G., 2021, [ApJ](#), **919**, 52

APPENDIX A:

This paper has been typeset from a \LaTeX file prepared by the author.

Table A1. Derived offsets of our photometric data.

Cluster	ΔV	$\Delta(V - R)$	$\Delta(V - I)$	$\Delta(V - R)$	$\Delta(V - I)$	$\Delta(B - V)$
Basel 4	-0.02(0.04)	-0.03(0.03)	-0.05(0.04)	-0.09	-0.06	-0.02
Berkeley 35	+0.01(0.02)	+0.02(0.02)	-0.00(0.02)	+0.01	+0.00	-0.04
Berkeley 60	-0.02(0.04)	+0.03(0.04)	-0.04(0.04)	-0.05	-0.04	+0.00
Berkeley 77	-0.02(0.02)	-0.03(0.02)	-0.01(0.03)	-0.02	-0.01	-0.01
Berkeley 104	-0.00(0.02)	+0.02(0.02)	-0.02(0.02)	-0.03	-0.03	-0.04
Haffner 4	-0.00(0.03)	+0.02(0.04)	-0.01(0.03)	-0.01	-0.01	-0.09
King 15	+0.02(0.02)	+0.02(0.02)	-0.00(0.03)	-0.02	-0.01	-0.04
King 23	-0.01(0.02)	+0.00(0.02)	-0.03(0.03)	-0.01	+0.00	-0.02
NGC 1857	-0.00(0.02)	+0.02(0.02)	-0.03(0.03)	-0.02	-0.03	-0.05
NGC 2186	+0.00(0.03)	+0.00(0.03)	-0.04(0.04)	-0.03	+0.00	-0.04
NGC 2236	-0.00(0.02)	+0.02(0.02)	-0.02(0.02)	-0.02	-0.02	-0.04
NGC 2259	+0.00(0.02)	+0.02(0.02)	-0.04(0.02)	-0.02	-0.04	-0.06
NGC 2304	+0.02(0.02)	+0.01(0.02)	+0.02(0.02)	+0.01	+0.02	-0.02
NGC 2383	-0.01(0.02)	-0.01(0.03)	-0.01(0.02)	-0.03	-0.01	+0.00

Notes. The first three columns list the difference of transformed *Gaia* photometry minus ours; the remaining columns give the derived offsets by obtaining a common temperature scale. All values are given in magnitudes, and the standard deviation is given in parentheses.

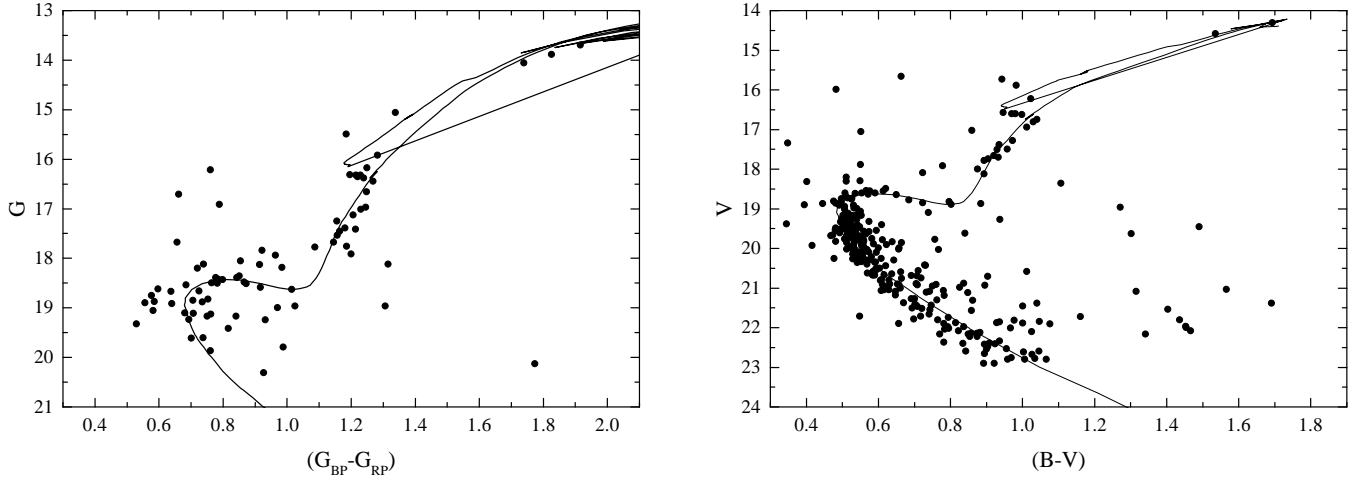


Figure A1. Result for the open cluster Berkeley 29. The left-hand panel shows the *Gaia* CMD of proper motion members and the right-hand panel the *BV* data by Tosi et al. (2004) restricted to the innermost cluster region. The overplotted isochrones correspond to the parameters listed in Table 3.

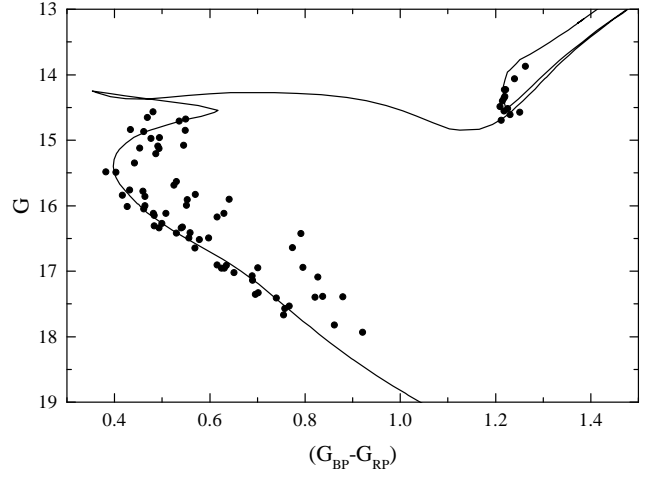
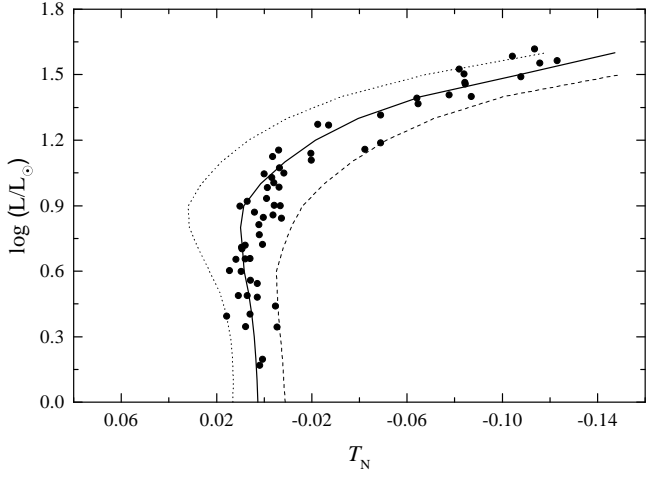


Figure A2. As Figure 2, but for Berkeley 35.

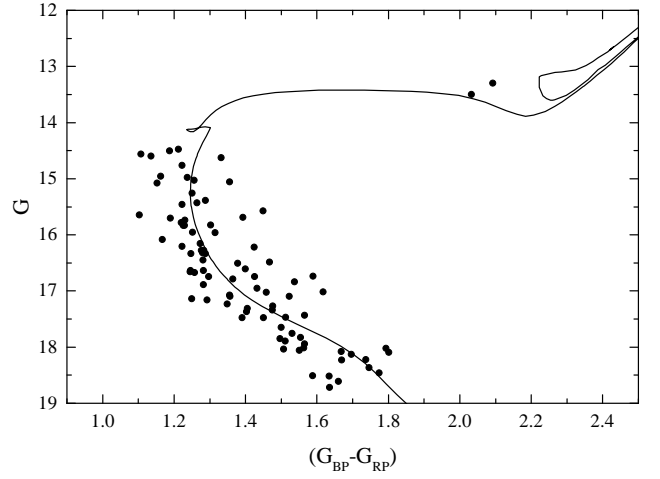
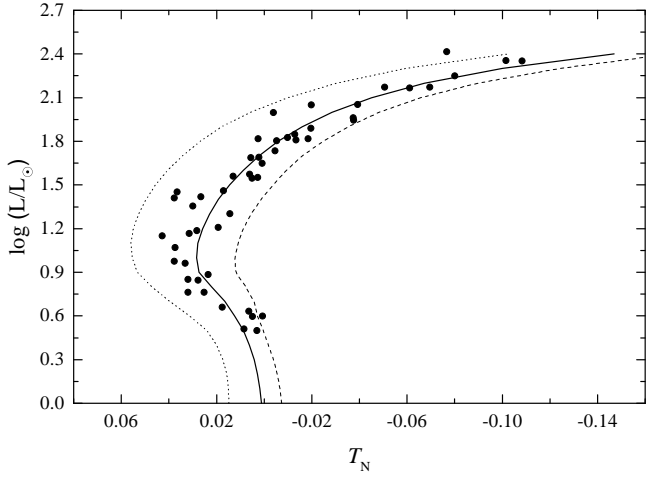


Figure A3. As Figure 2, but for Berkeley 60.

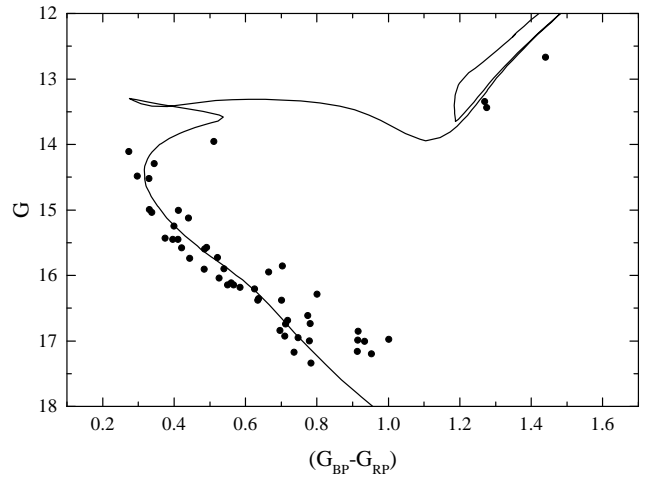
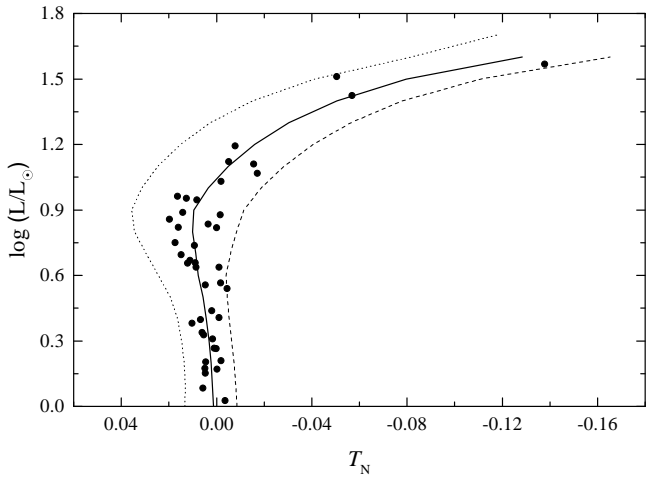


Figure A4. As Figure 2, but for Berkeley 77.

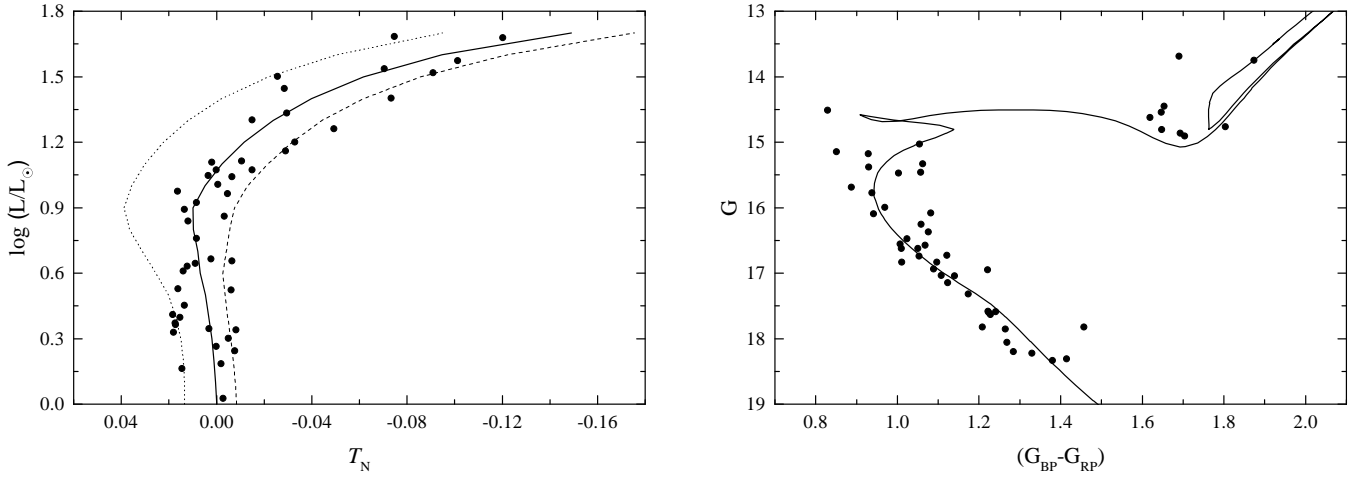


Figure A5. As Figure 2, but for Berkeley 104.

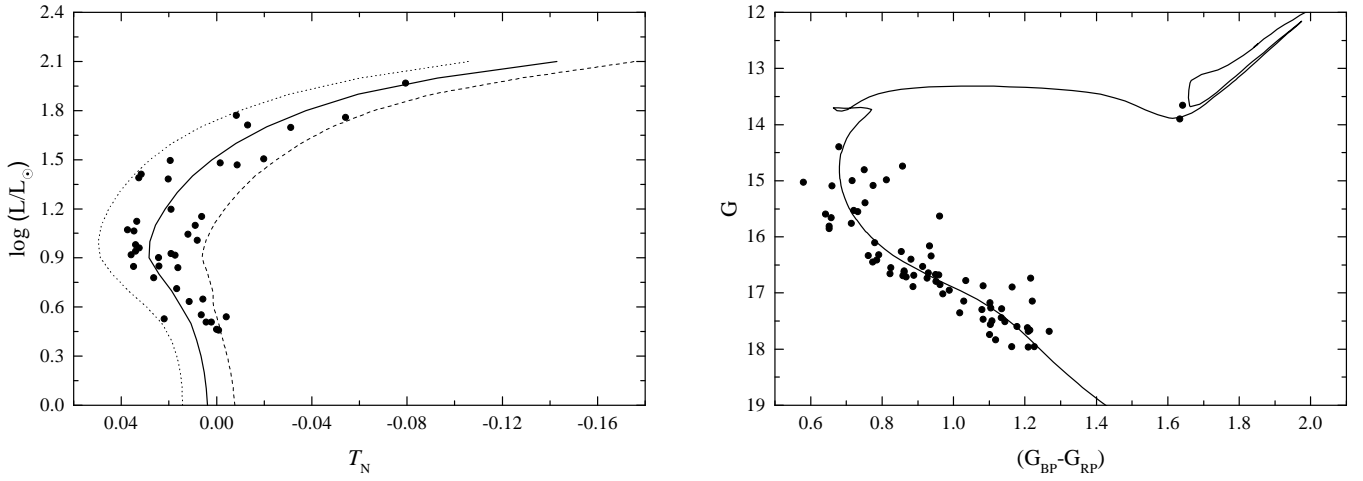


Figure A6. As Figure 2, but for Haffner 4.

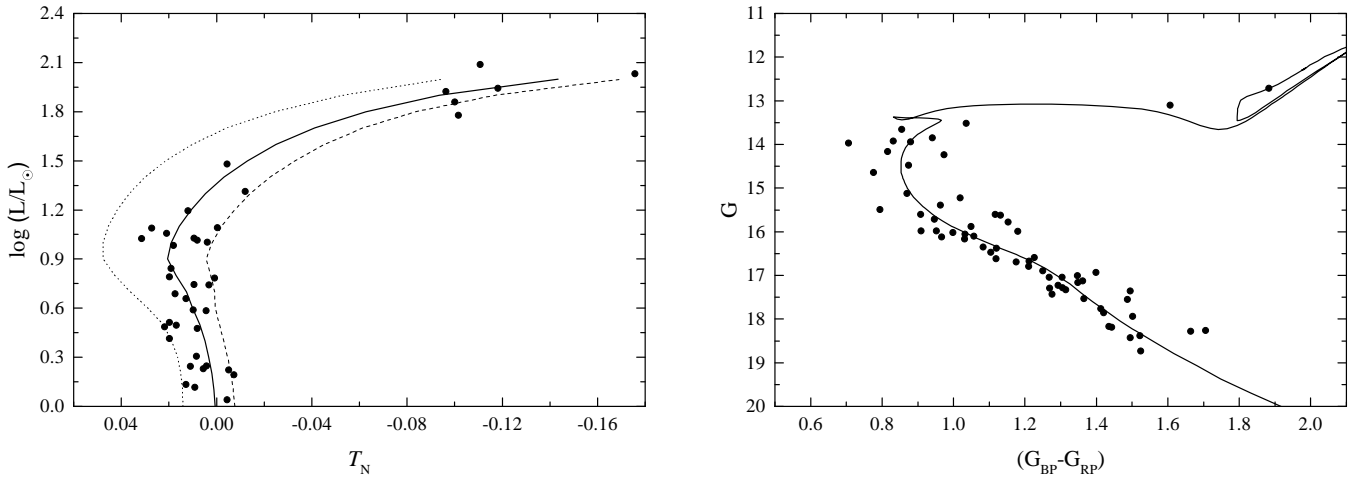


Figure A7. As Figure 2, but for King 15.

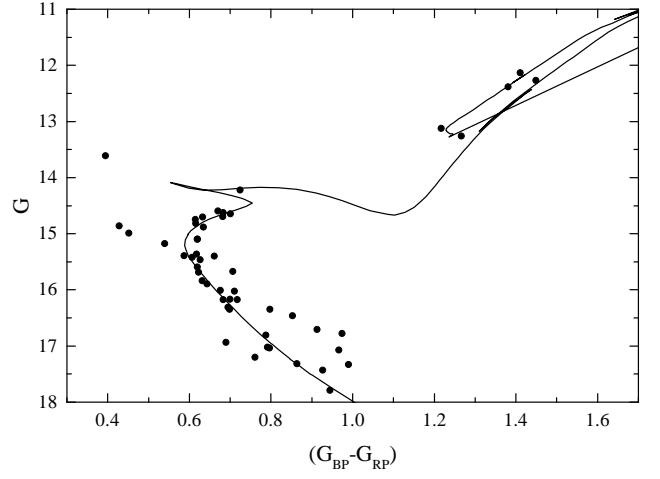
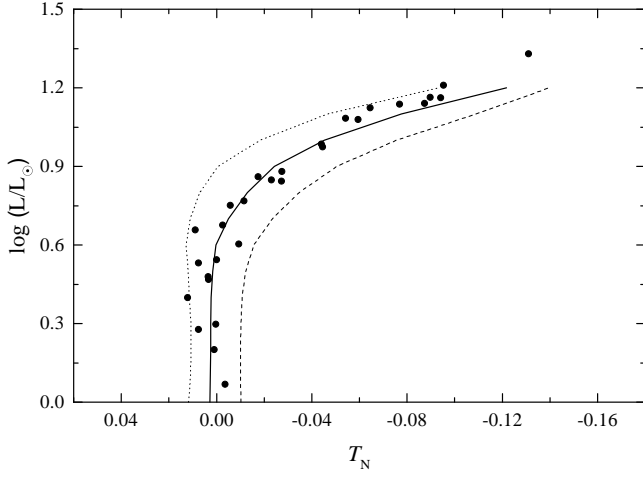


Figure A8. As Figure 2, but for King 23.

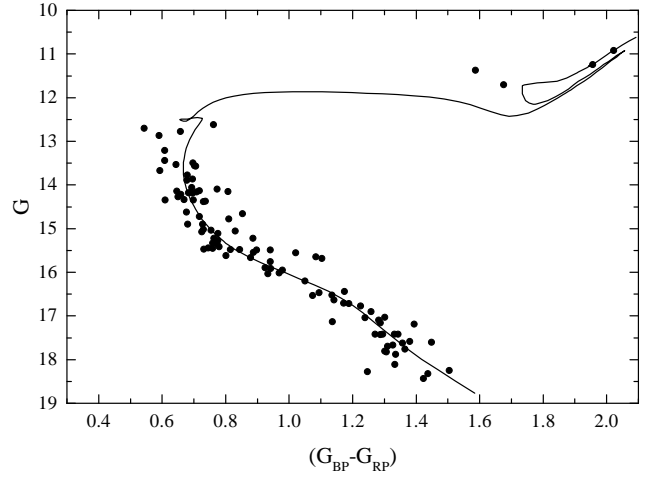
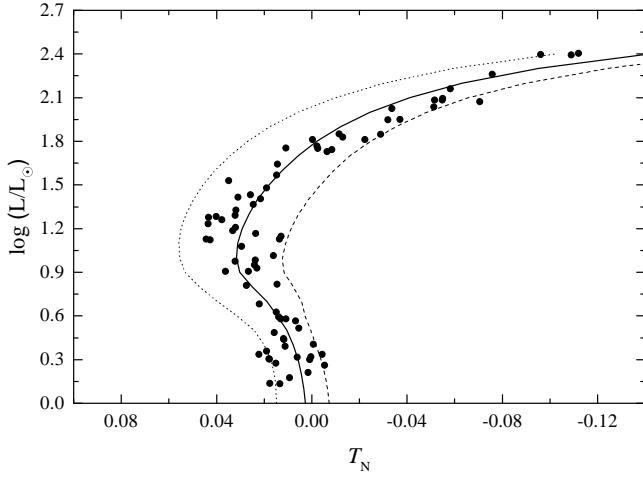


Figure A9. As Figure 2, but for NGC 1857.

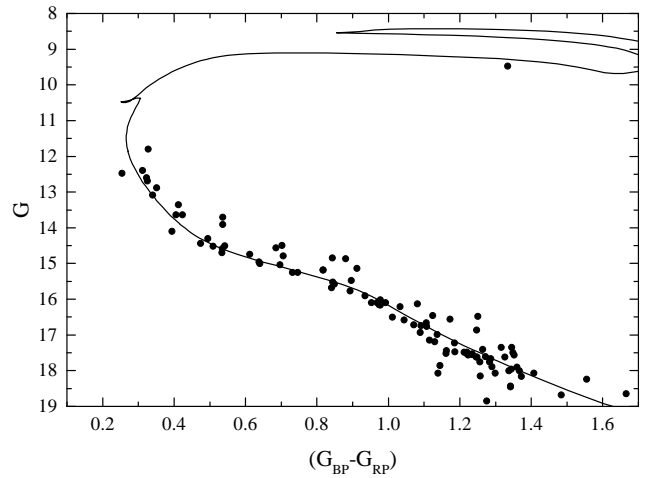
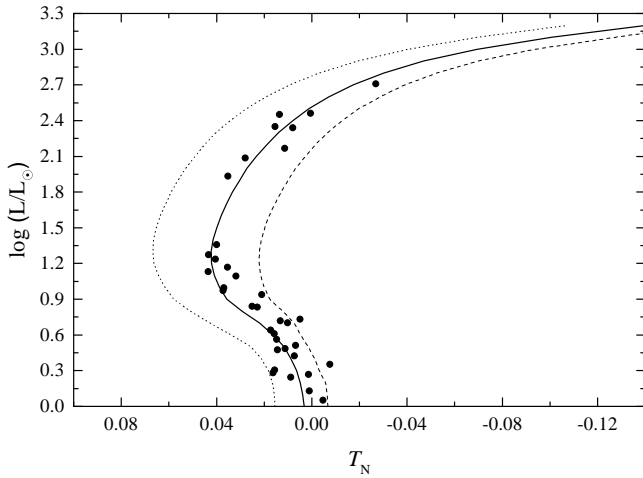


Figure A10. As Figure 2, but for NGC 2186.

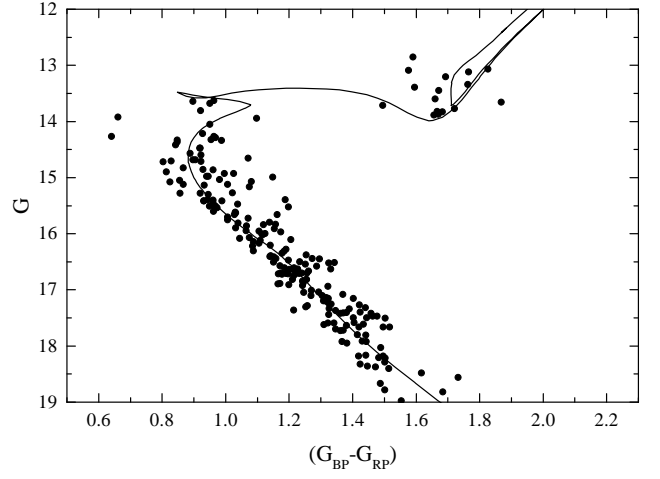
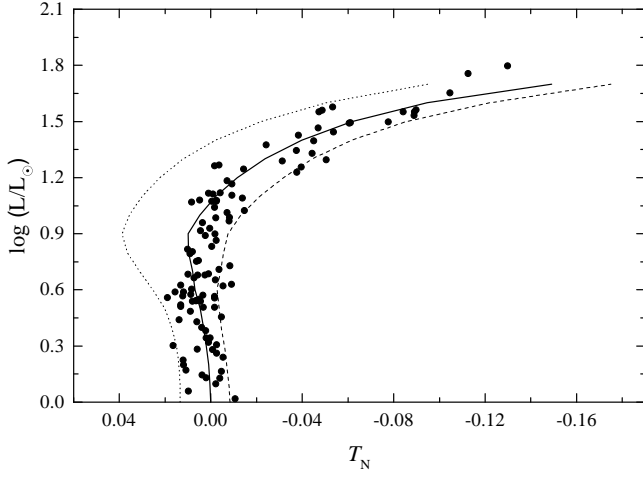


Figure A11. As Figure 2, but for NGC 2236.

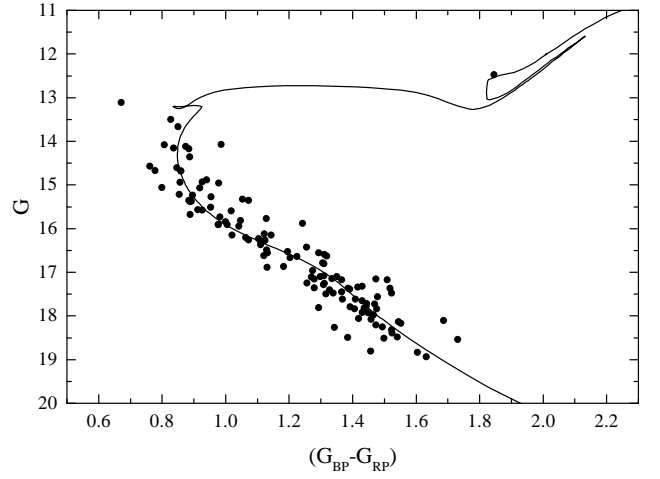
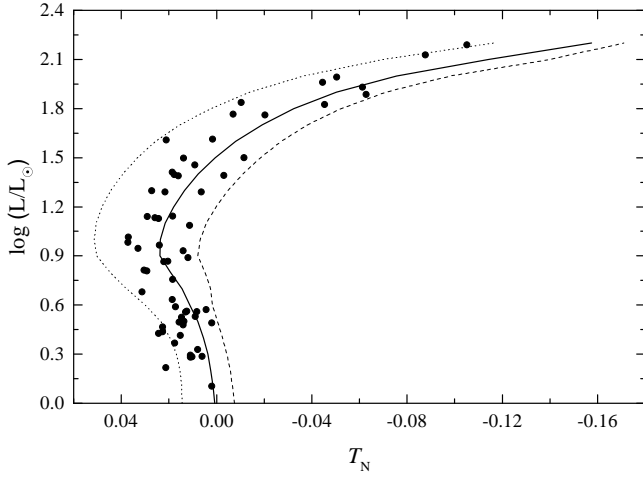


Figure A12. As Figure 2, but for NGC 2259.

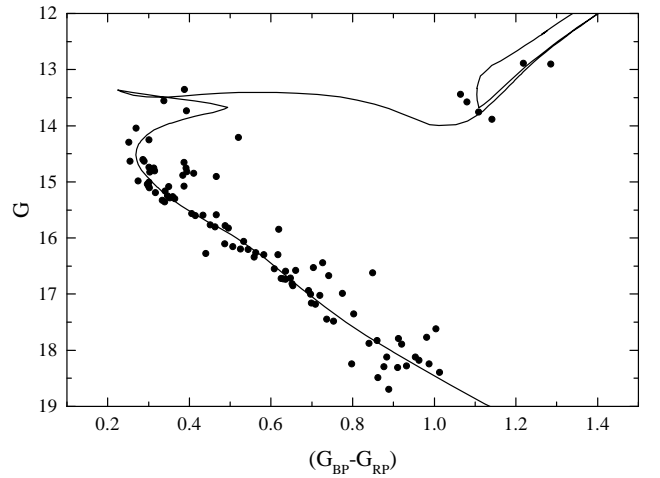
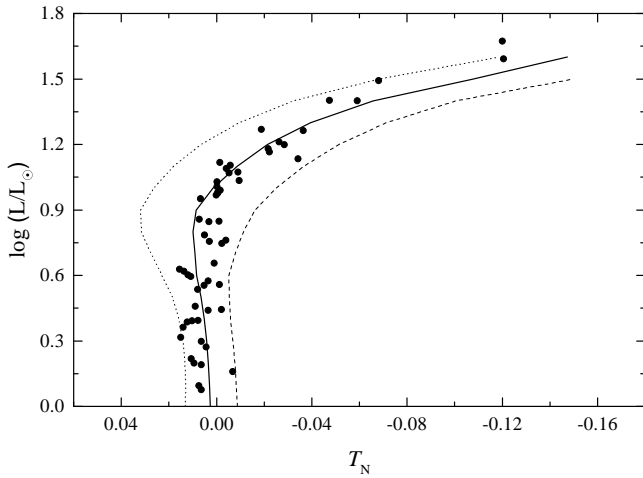


Figure A13. As Figure 2, but for NGC 2304.

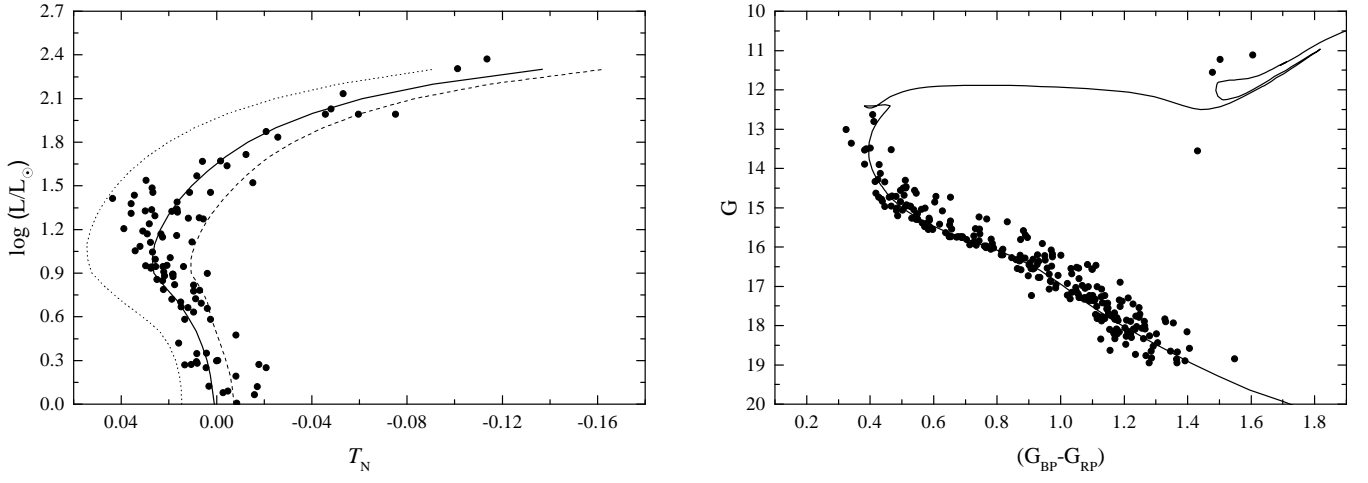


Figure A14. As Figure 2, but for NGC 2383.